UCRL 9841

University of California

Ernest O. Lawrence
Radiation Laboratory

PHOTOPRODUCTION OF π^+ IN HYDROGEN

Berkeley, California

DISCLAIMER

UCRL-9841
UC-34 Physics
TID-4500(17th Ed.)

UNIVERSITY OF CALIFORNIA
Lawrence Radiation Laboratory
Berkeley, California

Contract No. W-7405-eng-48

PHOTOPRODUCTION OF π^+ IN HYDROGEN

Donald A. McPherson
(Ph. D. Thesis)

October 19, 1961

Printed in USA. Price $2.00. Available from the
Office of Technical Services
U. S. Department of Commerce
Washington 25, D.C.

PHOTOPRODUCTION OF π^+ IN HYDROGEN

Contents

PHOTOPRODUCTION OF π^+ IN HYDROGEN

Donald A. McPherson

Lawrence Radiation Laboratory
University of California
Berkeley, California

October 17, 1961

ABSTRACT

Differential cross sections for photopion production from protons were measured for 32 photon energies from 154 to 185 Mev with the 4-in. liquid-hydrogen bubble chamber and the Berkeley electron synchrotron. High photon intensities of 1.5×10^7 Mev/pulse were used by collimating the beam down to a narrow "ribbon" which was viewed on edge by the camera. Although the pion origins were obscured by the heavy electron background, the remainder of the pion track was visible for most events. Of 5000 π- μ decays seen, 3400 were deemed suitable for calculations.

The results are in excellent agreement with the theoretical calculations of Ball who applied the Mandelstam representation to the process. The combined measured cross sections, averaged over the pion c.m. angles, for photon energies of 154, 157, 162, 167, 172, 177, and 182 Mev are 2.71 ± 0.78, 3.48 ± 0.12, 4.62 ± 0.14, 6.07 ± 0.22, 6.47 ± 0.31, 5.74 ± 0.43, and 6.37 ± 0.71 μb/Mev-sterad respectively. All data are subject to an additional correlated error of 4.1% because of the uncertainty in the beam normalization. Also a value of $\Lambda = (-0.397 \pm 0.552)e$ was obtained, where Λ is the multiplicative factor associated with the matrix element for photopion production from pions as calculated by Wong.

I. THEORY

A. Introduction

The latest theoretical work in photopion production is the application of dispersion relations. The series of papers by Chew and his associates are discussed in order to obtain an integral picture of the progress of this theory.[1-6]

In 1957, Chew and Low evaluated the photoproduction amplitude to order $1/M$ (M = nucleon mass), assuming a nonrelativistic Yukawa interaction between the pion and nucleon and the dominance of the 3-3 resonance in final-state scattering.[1] Chew, Goldberger, Low, and Nambu (CGLN) generalized this treatment by forming Lorentz- and gauge-invariant amplitudes expressed in terms of fixed-momentum-transfer dispersion relations.[2] Finally Ball[3] extended the CGLN formalism, using the double spectral representation of Mandelstam. These three papers are discussed briefly below.

B. Interaction Approach

Chew and Low calculated the amplitudes nonrelativistically by using the interaction Hamiltonian

$$H = -\int \underset{\sim}{j} \cdot \underset{\sim}{A} \; d \; \underset{\sim}{r} . \qquad (1)$$

They considered the nucleon mass heavy enough so that nucleon recoil is negligible. The current $\underset{\sim}{j}$ is broken into a sum

$$\underset{\sim}{j} = \underset{\sim}{j}_{\pi} + \underset{\sim}{j}_{N} . \qquad (2)$$

The current $\underset{\sim}{j}_{N}$ is supposed to be independent of the meson field, and gives rise to meson production only from the magnetic moment of the nucleon because there is no nucleon-recoil term. Parity and angular-momentum considerations show that this is a magnetic-dipole interaction with the final state having orbital angular momentum one. Part of this state has I-spin 1/2 and part has I-spin 3/2. It is assumed

that the 3-3 phase shift dominates all others, so that only final-state scattering in the 3-3 state is considered.

The current j_π gives rise to the interaction between the meson cloud and the photon. Near threshold, the most important production is by electric dipole into an S-wave state. At threshold, this is the only mechanism for production. Chew and Low were not able to evaluate secondary scattering for this amplitude because the 3-3 final state is not involved in the S-wave dipole term and because the other phase shifts were not well-known at this energy.

C. Dispersion Relations

The generalization by CGLN led to a cross section similar in appearance to that of Chew and Low, the most significant addition being an anomalous magnetic-moment electric-dipole term. The final-state scattering contributions in the S-wave electric-dipole production were still excluded.

The treatment by Ball using double-dispersion relations resulted in essentially the same result as that obtained by CGLN except that a term related to the photopion production from a pion was added to the amplitude.[3] Using methods characteristic to the application of the Mandelstam representation, Ball postulates that the amplitudes representing the reactions

$$\gamma + N \rightarrow N + \pi,$$
$$\gamma + \bar{N} \rightarrow \bar{N} + \pi, \qquad (3)$$

and

$$\gamma + \pi \rightarrow N + \bar{N}$$

are representations of a single set of functions that can be expressed in terms of the two-dimensional Mandelstam representation. By virtue of this common representation, there are contributions to the channel $\gamma + N \rightarrow \pi + N$ from the other two channels. According to Chew, these contributions are dominated by the intermediate states of lowest energy. For instance, the reaction $\gamma + \pi \rightarrow N + \bar{N}$ is

considered in the form

$$\gamma + \pi \rightarrow \pi + \pi \rightarrow N + \bar{N}, \tag{4}$$

where the π, π system is the intermediate state with the lowest energy. Wong has studied the $\gamma + \pi \rightarrow \pi + \pi$ problem and concludes that at low energy, the major contribution comes from magnetic-dipole production into the state $\ell = 1$, $I = 1$, where ℓ and I are orbital angular momentum and isotopic spin.[4] Because he had to neglect inelastic processes, Wong obtained a homogeneous integral equation for this magnetic-dipole amplitude M_1 which required him to introduce a multiplicative constant Λ. Using the pole approximation of Chew and Mandelstam, Wong expressed M_1 in "one-pole" and "two-pole" formulas. The "one-pole" formula is

$$M_1(s) = \Lambda \frac{(1+a)}{(s+a)} \frac{D_1(1)}{D_1(s)} \quad ; \quad M_1(1) \equiv \Lambda, \tag{5}$$

where s is the center-of-mass energy, and $D_1(-a)/D_1(s)$ is the pion form factor obtained by Frazer and Fulco.[5] The parameter $(-a)$ is the location of the effective pole on the real axis and is given by Wong as $a \simeq 5.7$.

Frazer and Fulco have studied the remaining process, $\pi + \pi \rightarrow N + \bar{N}$.[6] Using a one-pole approximation, they were able to express the amplitude in explicit form.

By combining these results, Ball was able to calculate the contributions from the $\gamma + \pi \rightarrow N + \bar{N}$ channel. In addition he was able to avoid the $1/M$ expansion used by CGLN; however, he still did not include the secondary scattering effects in the S-wave state. If M' is the amplitude for production without the π-π effect, then according to Ball the π-π interaction produces a fractional change of $1 + (0.074\ \Lambda/e)$ in $|M'|^2$, where e is the electronic charge.

II. EXPERIMENTAL TECHNIQUE

A. Characterizing Features

The data of this experiment are embodied in 180,000 bubble chamber photographs taken with the 4-in. liquid-hydrogen bubble chamber set up in the bremsstrahlung beam of the Berkeley electron synchrotron. Photopions produced by 153- to 186-Mev photons were observed.

The feature that characterized this experiment is the thin rectangular shape of the beam profile which was viewed on edge by the camera. This permitted use of a beam intensity fifteen times as large as those intensities used in previous photoproduction experiments.[7] Miller and Hill originated this technique.[8]

Figure 1 is a photograph of a π-μ decay. The effect of using a high-intensity beam was to mask the entire center portion of the chamber with a ribbon of bubbles created by the large number of electrons produced in the forward direction. However the π-μ decay is clearly visible and the uncertainty in the origin of the pion is only the half width of the beam, 0.20 cm. This corresponds to an uncertainty of $\pm$ 0.4 Mev for a 5-Mev pion.

B. Synchrotron Operation

The energy of the synchrotron beam was fixed by setting the voltage on the capacitor bank at 8.73 kv. This corresponded to a peak energy in the bremsstrahlung beam of 189.1 $\pm$ 3.7 Mev, as will be shown in Sec. VII. The error arises entirely from the measurement of the peak energy. The radiofrequency envelope was adjusted so that the beam fallout occurred at peak magnetic field and lasted 20 μsec. The fallout duration of 20 μsec was small compared to the 1.2 msec allowed for bubble growth. Signals corresponding to beam fallout and peak field were monitored continually and were never separated by more than 100 μsec. This corresponded to a shift in peak energy of 0.4 Mev and, for the most part, the time difference was much less.

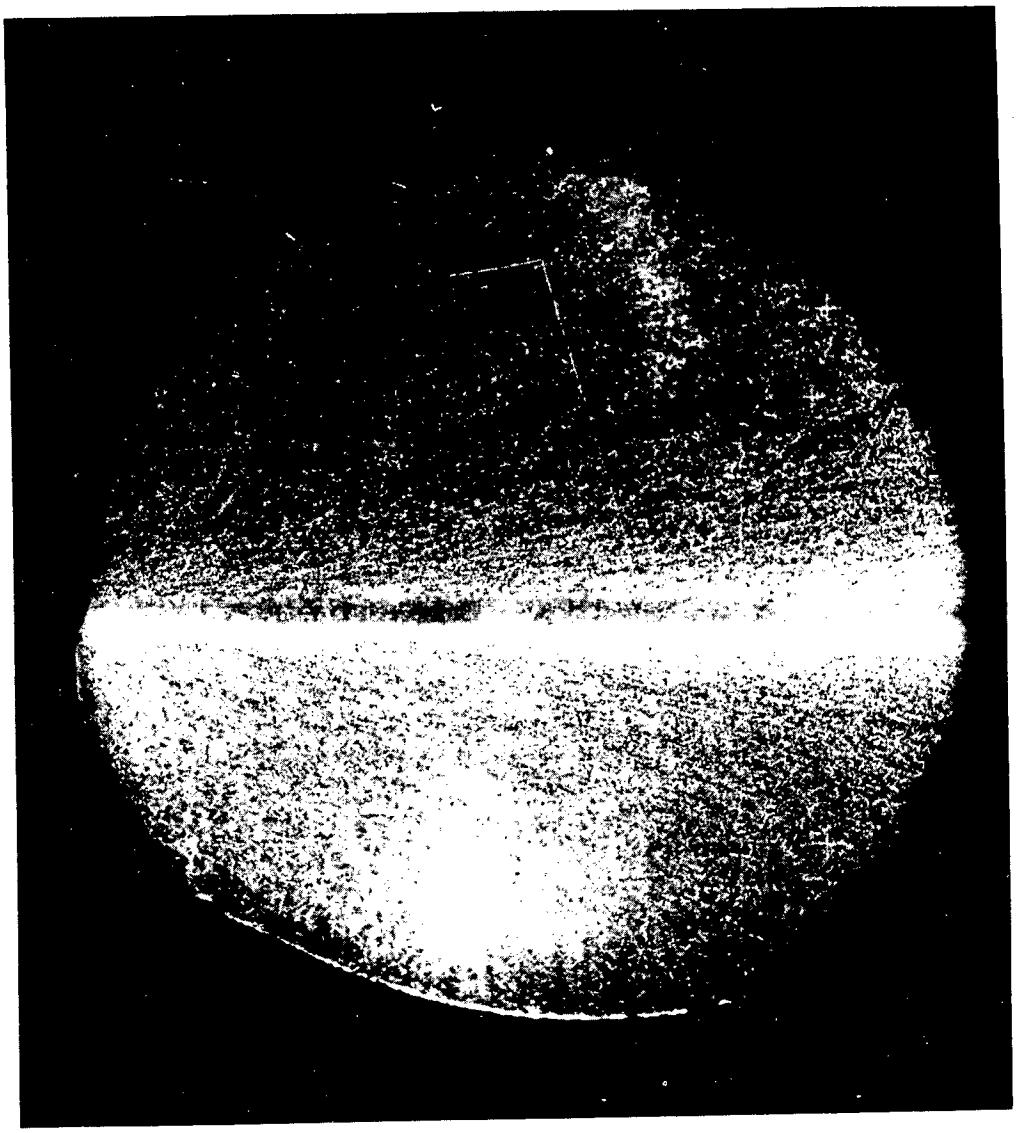

ZN-2977

Fig. 1. A π- μ decay. Background is so heavy at the center that it blanks out the light and causes the dark streak at the beam region. The beam enters from the left.

Most of the film was exposed using a beam intensity of 1.5×10^7 Mev/pulse. Film exposed at an intensity of 2.0×10^7 Mev/pulse showed a marked increase in electron background and was not suitable for detecting photopions produced by photons of less than 160-Mev energy.

C. Beam Geometry

1. Introduction

Figure 2 shows the arrangement of the experimental apparatus. In order to obtain a high beam intensity, the bubble chamber was moved as close to the synchrotron as possible. The distance from the synchrotron target to the chamber 148 inches--was occupied entirely by the following components which were necessary to obtain the desired beam characteristics:

1. collimators
2. magnets to sweep out charged particles
3. lithium hydride to absorb low-energy photons
4. ionization chambers to monitor the beam.

2. Collimators

Three collimators shaped the beam profile. These were lined up on the beam by means of a telescope which previously had been aligned by exposing x-ray films at the telescope. The first two collimators were brass-lined, 1/4-in. -diam. tapers which allowed the beam to pass through the external shielding of the synchrotron. The third collimator was the slit which gave the beam its characteristic "ribbon" shape. The distance between the synchrotron target and the slit collimator was 97.5 in. The slit was 6 by 0.305 by 0.090 in., with a 9-deg taper in the 0.305-in. dimension. The beam in the chamber was 0.669 by 0.145 in. Figure 3 shows a photograph of this collimator.

3. Magnets

A clean electron-free photon beam was obtained by using two identical magnets to sweep charged particles out of the beam. These were positioned side by side behind the second collimator, with the slit collimator resting on the pole face of the second magnet.

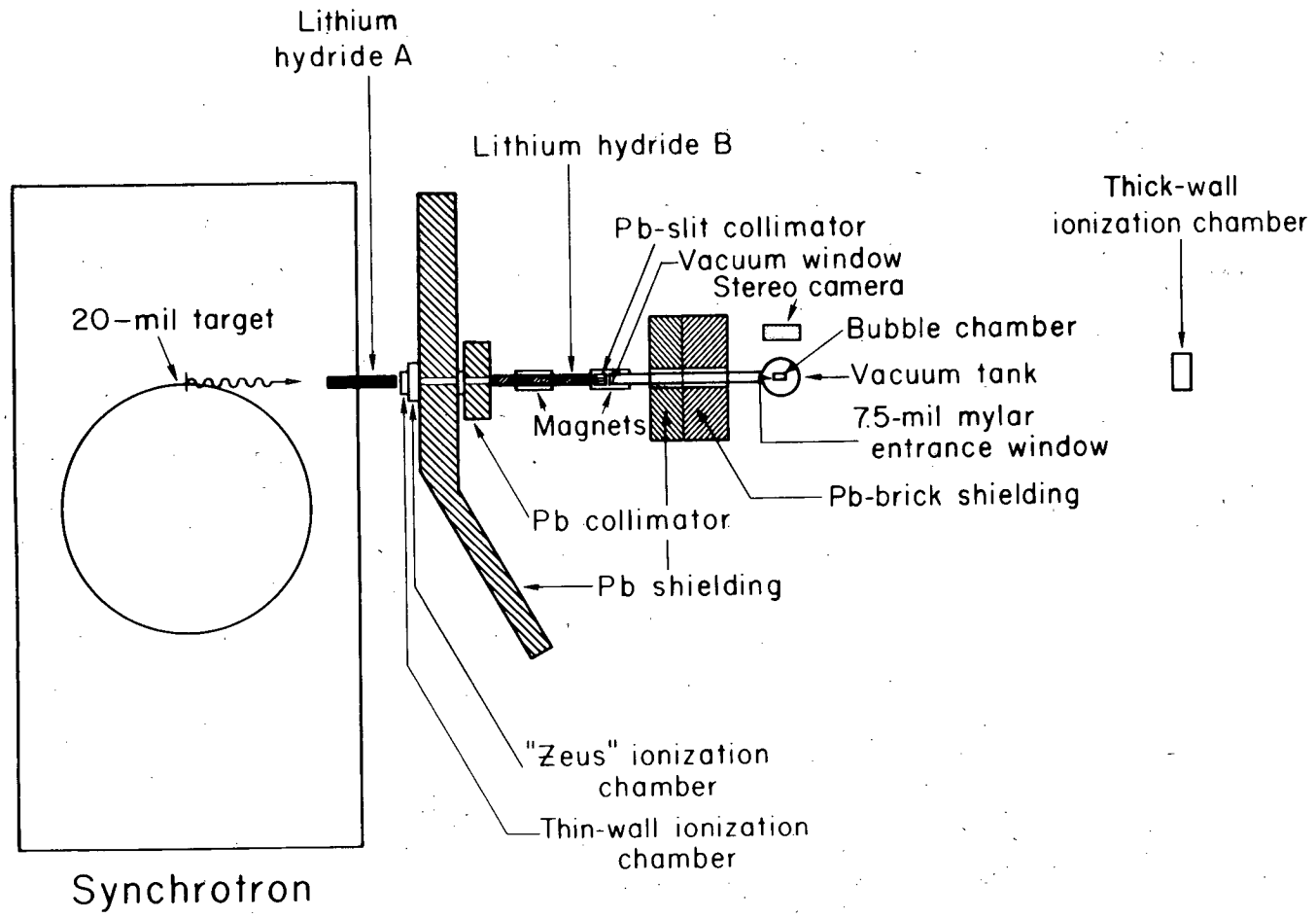

Fig. 2. Experimental setup for film taking. Beam leaves the synchrotron on the left and is "hardened" by the tubes of lithium hydride, A and B. After being collimated by the slit collimator, it enters the vacuum system of the bubble chamber. The thick-wall Cornell ionization chamber which monitored the beam is on the far right.

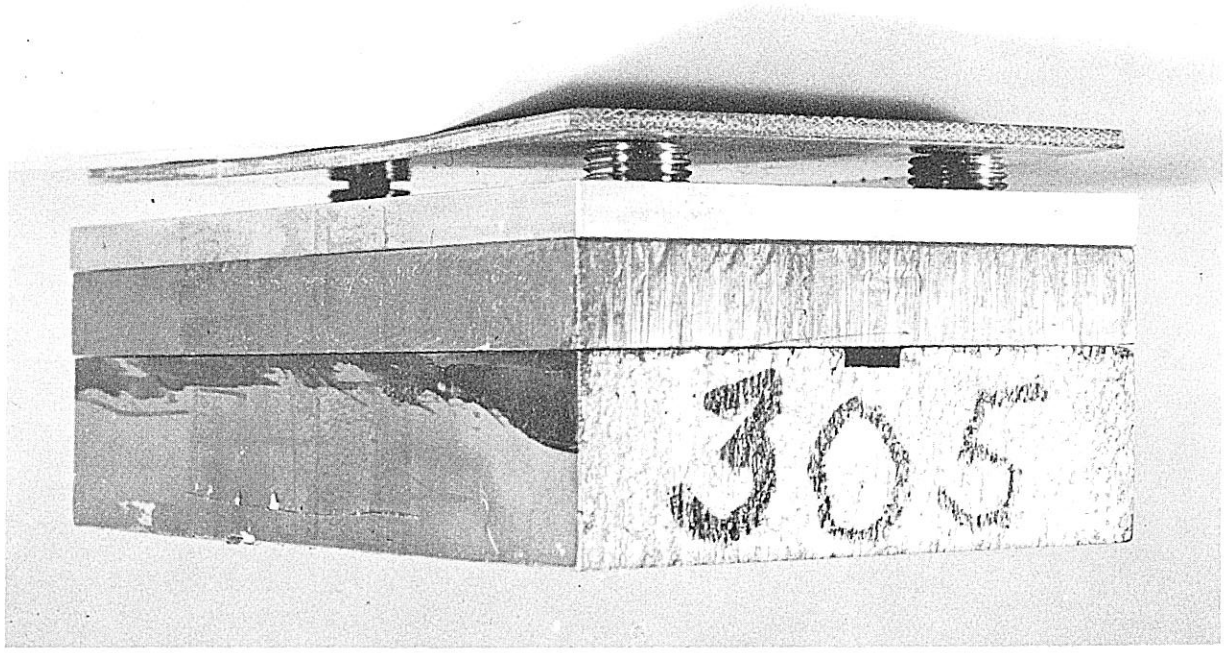

ZN-2976

Fig. 3. The slit collimator.

The bubble-chamber vacuum was extended from the bubble-chamber tank through a 2-ft-thick lead wall to the slit collimator by means of a 2-1/4-in.-diam brass tube. After being collimated by the slit, the beam entered this vacuum through a 1/2-in. Lucite window and encountered no further material until it passed through the 7-mil Mylar window in the chamber wall. The first 7 inches of the vacuum extension was in the magnetic field of the second sweep magnet. Thus a 200-Mev electron produced in the end of the vacuum extension was deflected sufficiently to strike the lead shielding built about the vacuum extension tube.

4. Lithium hydride beam hardener

Because the bremsstrahlung spectrum is continuous, there were photons of all energies from zero to peak energy in the initial beam. Those below 150 Mev could not produce pions but could contribute to the electron background. Therefore it was advantageous to reduce the number of low-energy photons, that is, to "harden" the beam. A material with low atomic number, Z, was used because the pair-production process, which has a high cross section for high-energy photons, is dependent upon Z^2, whereas Compton scattering, which absorbs low-energy photons, is proportional to Z.

The low-Z material used was crushed lithium hydride packed in 2-in.-diam Lucite tubes. Two tubes denoted as B in Fig. 2 were both 2-1/2-ft-long and were placed in the sweep magnets between the second collimator and the slit collimator. Another tube denoted as A was 20-in.-long and was placed between the synchrotron exit window and the first collimator. Including the 5/32-in. end-pieces of the tubes, a total of 59.9 gram/cm^2 of low-Z material was placed in the beam path.

In Sec. VII, it will be shown that the transmission of 150- to 180-Mev photons through the LiH is 0.512. Although we did not measure the transmission for all energies in this experiment, we know from a previous experiment that the transmission remains nearly constant down to 80 Mev and then begins to decrease rapidly.[9] Using Fig. 10

of Ref. 9 and our transmission of 0.512 at 160 Mev, we find that for energies k = 40, 20, 10, and 1 Mev the transmissions were 0.473, 0.385, 0.222, and 0, respectively.

5. Ionization chambers

After leaving the bubble chamber, the beam passed through 10 ft of air and then struck a thick-wall ionization chamber of the type developed at Cornell.[10] This ionization chamber was the primary monitor of the beam. The charge from the Cornell chamber was collected on a 0.00994-μf capacitor. The voltage across the capacitor was fed into a 100%-feedback electrometer, which in turn drove a Leeds and Northrup recorder. The amplification of the electrometer and the recorder were set so that 1 volt across the capacitor corresponded to full scale on the recorder.

Two thin-wall ionization chambers used as secondary monitors were mounted in front of the first collimator. The use of these ionization chambers and the method for obtaining the amount of beam which passed through the bubble chamber is described in Sec. VII.

D. Bubble Chamber Operation

1. Description

A detailed description of the Alvarez 4-in.-diam. liquid-hydrogen bubble chamber can be found in Ref. 11, and operation in high-energy photon beams is described in Ref. 7. Figure 4 shows a close-up of the chamber itself. The most notable feature is the window through which the beam enters. This is a 13/16-in. diam. circular port, covered by a 7.5-mil film of Mylar. Thus the beam entered the hydrogen without creating a large electron background in the entrance window. The window is clearly visible on the right in Fig. 4.

2. Alignment of the beam

The dimensions and position of the slit collimator were chosen so that the rectangular-shaped beam was not wider than the entrance window of the bubble chamber. In Sec. IV it is shown that the beam was 1.7 cm or 0.669 inches wide. This left 1/16-inch clearance on either side and required that the chamber be precisely aligned to prevent the beam from striking the window edges.

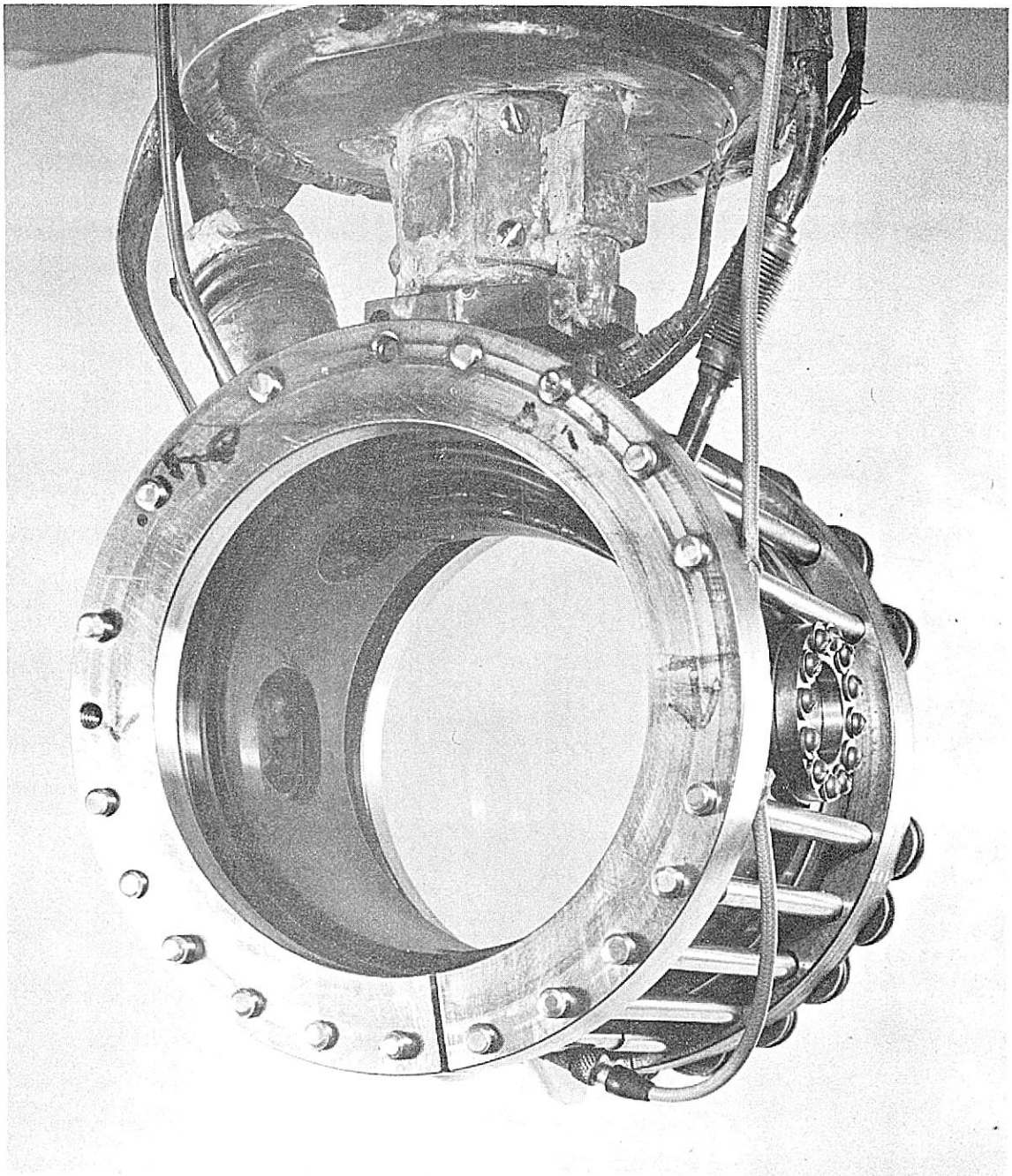

ZN-2518

Fig. 4. The bubble chamber removed from the vacuum system and heat shielding. Note the beam entrance window on the right.

For this alignment, x-ray photographs were taken of a lead cross centered on the entrance window and the position of the chamber was adjusted until the cross appeared superimposed on the beam. Figure 5 is such an x-ray exposure and Fig. 6 is a photograph of the window and lead cross. After the chamber was positioned, the cross was swung out of the way by means of a coupling through the vacuum jacket of the bubble chamber.

3. Operating conditions

The chamber was operated so that the ionization of single electrons was insufficient for bubble growth, although the more heavily ionizing pions left visible tracks. This level of bubble growth versus ionization was achieved by adjusting the temperature, pressure, and timing.

The pulsing of the chamber was governed by a Flex-O-Pulse timer set to cycle every 6 sec. At the beginning of the cycle, a signal that accompanied every synchrotron pulse was selected to initiate a chain of events which sensitized the chamber for the following synchrotron pulse. Figure 7 shows the sequence of events. About 156 msec after receiving the synchrotron signal, the chamber was expanded. The expansion period was 8 msec and the beam passed through the chamber 2.8 msec later. The bubbles were allowed to grow for 1.2 msec, and then the strobe lamps were flashed to expose the film. Next an auxiliary lamp was flashed to record the frame number, and the film was wound.

Table I gives the operating conditions along with those of the 10-in. chamber for comparison.[12] Because the temperature and initial pressure of the 4-in. chamber were higher than those of the 10-in. chamber, in order to have biased out electron tracks, the post-expansion pressure must have been greater than the 48 psia post-expansion pressure of the 10-in. chamber. The pressures and temperatures for this experiment, quoted in Table I of Ref. 7, should be replaced by the values in Table I.

ZN-2975

Fig. 5. An x-ray of the beam taken with the beam aligning cross in position. Note the faint light cross mark centered on the beam.

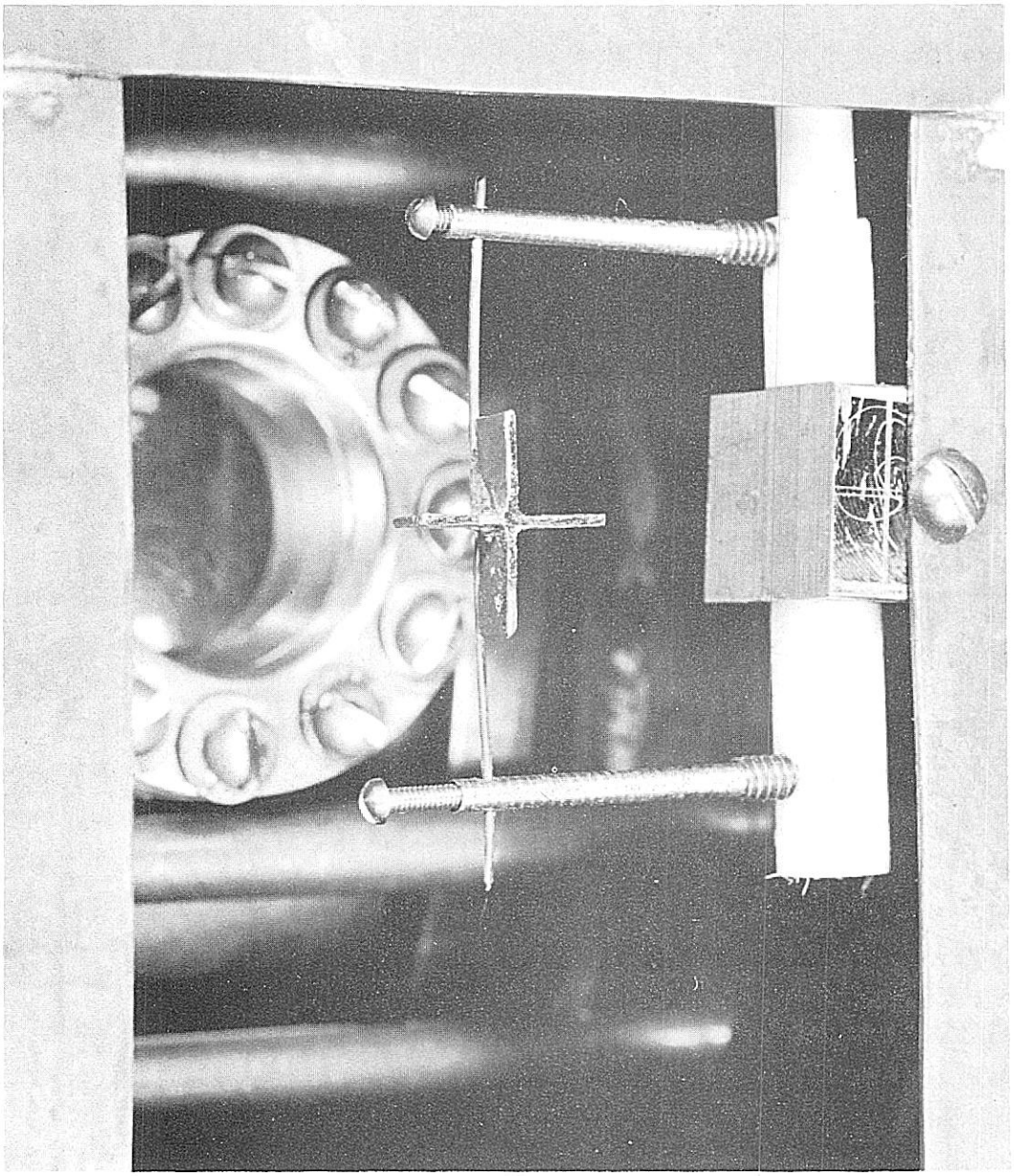

ZN-2517

Fig. 6. The beam aligning cross swung into position in front of the entrance window. The cross is swung out of the beam when data are taken.

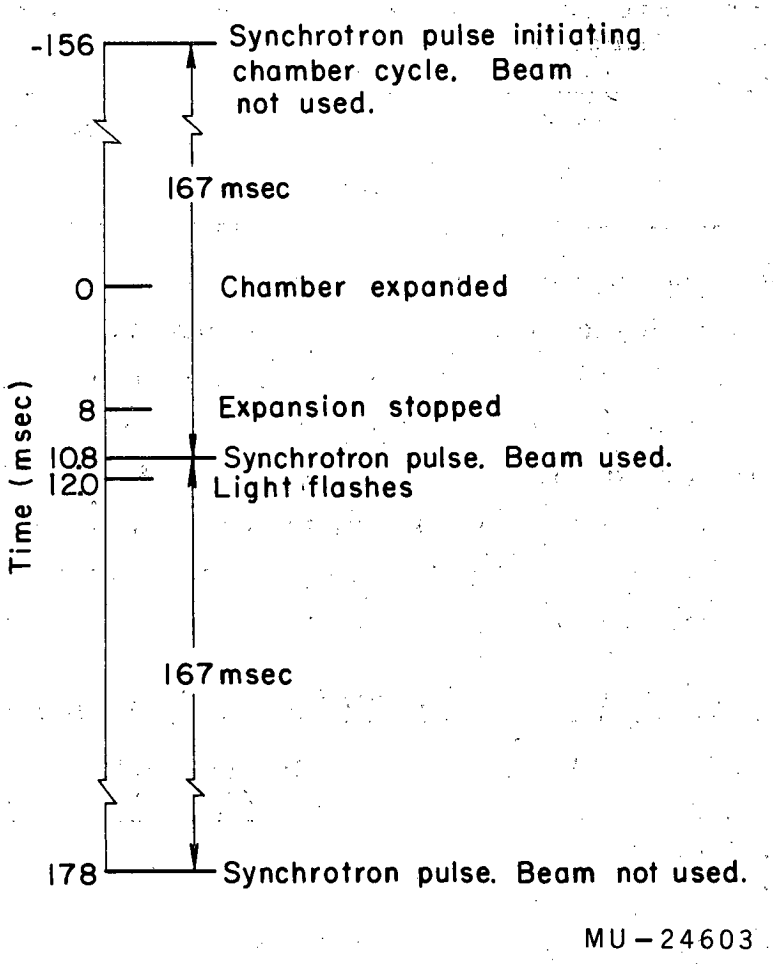

Fig. 7. Sequence of events for one chamber cycle. Read from top to bottom.

Table I. Operating conditions of the 4-inch bubble chamber. Those of the 10-inch chamber are given for comparison.

Chamber diameter (in.)	Pre-expansion temperature (°K)	Pre-expansion pressure (psia)	Post-expansion pressure (psia)	Density (gm/cm^3)
4	29.5	115	not measured	0.0552
10	27.9	85	48	0.05940

4. Photographic technique

The photographic apparatus and chamber optics are illustrated in Fig. 8. To prevent shadows cast by the opaque ribbon of bubbles in the beam region, two GE FT-218 flash tubes displaced 1/2-in. from the center line of the optics were used. Uniform illumination of the chamber was achieved by varying the operating voltages of these flash tubes. Table II summarizes the operating conditions. The Kemlite FA-100 flash tube was used to register the frame number on the film.

Table II. Operating conditions of the light sources

Flash tube	Voltage (v)	Capacitance (μf)	Power (watt-sec)
FT-218 No. 1	680	10	2.3
FT-218 No. 2	380	15	1.1
FA-100 data light	420	80	7.0

Dark-field photography resulted from focusing the light sources between the camera lenses by means of the plano-convex lens shown in Fig. 8. The Recordak stereographic camera used 100-ft rolls of unperforated 35-mm Eastman Kodak Panatomic-X film, and the lens apertures were set at f/22, which gave excellent depth of field. The entire apparatus shown in Fig. 8 was enclosed in a housing sufficiently lighttight so that no shutter was required on the camera.

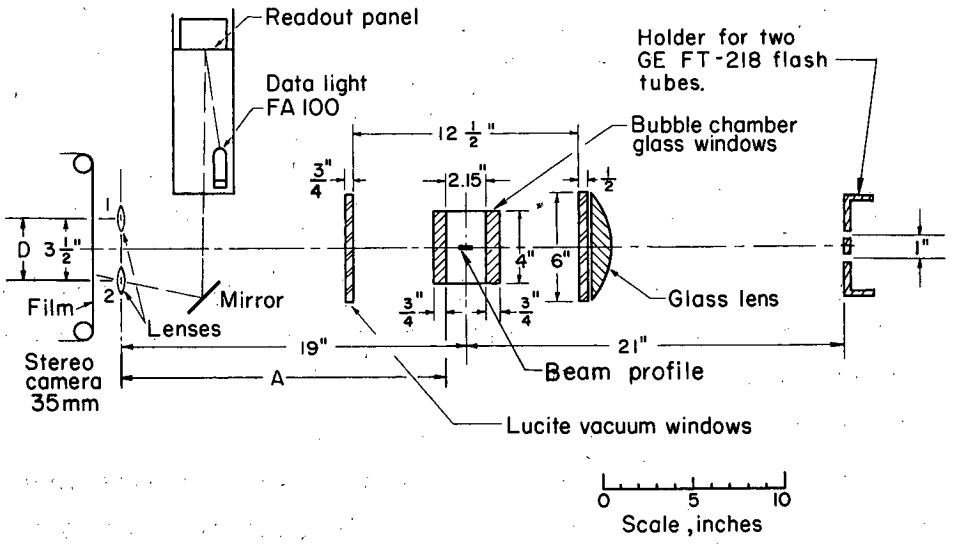

Fig. 8. Schematic of the optical system. The light from two flash tubes on the right is focused between camera lenses 1 and 2 on the left by the glass lens. Bubbles in the chamber scatter light into the camera lenses.

III. SCANNING AND MEASURING

A. Scanning

The film was scanned three times by a group of seven people using stereo scanning machines.

Our scanners were not infallible, and so a scanning efficiency factor must be incorporated into the cross section. If two people scan the same film, their scanning efficiencies will be

$$E_1 = \frac{N_{12}}{N_2 + N_{12}} \tag{6}$$

and

$$E_2 = \frac{N_2}{N_1 + N_{12}} \quad , \tag{7}$$

where N_{12} is the number of events seen by scanners 1 and 2, N_1 represents events seen by 1 but not by 2, and N_2 represents events seen by 2 but not by 1. We assume that the individual scanners are not biased against a certain type of event.

We had seven scanners and three scans, which constitutes 35 separate groups of scanners. By labeling the scanners, 1, 2, 3, 4, 5, 6, and 7, the groups can be tagged by an index j, where j = 1 represents scanners 1, 2, 3, j = 2 represents scanners 1, 2, 4, j = 33 represents scanners 4, 5, 7, j = 34 represents scanners 4, 6, 7, and j = 35 represents scanners 5, 6, 7.

The efficiency of scanner 1, generalized from Eq. (6), is

$$E_1 = \frac{\sum_j N_{123}^j}{\sum_j N_{23}^j + \sum_j N_{123}^j} \tag{8}$$

where N_{123}^j is the number of events seen by all three scanners of group j, and N_{23}^j represents events seen by the second and third members of group j but not by the first member. The index j is restricted to those 15 groups of which scanner 1 is a member.

We considered the possibility that scanning efficiencies would not be constant for various regions of the chamber. Therefore the chamber was divided into five regions on each side of the beam, and a scanning efficiency was calculated for each region. Figure 9 is a top view of the chamber with the diverging lines representing the vertical boundaries of the regions. The sectors on either side of the center were divided into upper and lower regions which were designated as 1 and 2, respectively. The next two sectors flanking these were likewise divided into upper and lower regions designated 3 and 4. Finally the two sectors on the outside were designated as region 5.

In this manner, scanning efficiency E_i^r was calculated for each scanner ($i = 1, 7$) for each region ($r = 1, 5$). The combined scanning efficiency in region r for a roll that had been scanned by scanners i, j, and k is

$$E^r(\text{roll}) = E_i^r + E_j^r + E_k^r + E_i^r E_j^r E_k^r - E_i^r E_j^r - E_i^r E_k^r - E_j^r E_k^r . \quad (9)$$

We used 3400 events to calculate the five regional scanning efficiencies for each roll of film. At most, the scanning efficiencies of two groups differed by 1%. A typical set of efficiencies for a roll are:

Region	1	2	3	4	5
Scanning efficiency	0.9962	0.9887	0.9976	0.9988	0.9998.

There is a slight trend downward from the outside region 5 to the inside regions 1 and 2. However, in view of the high efficiencies and this negligible trend, it is doubtful that the scanning efficiency need be evaluated in such detail. Individual scanner efficiences are given in Table III. Each event is weighted by the inverse of the scan efficiency of the roll and region in which the event was found. This is shown in Sec. VIII where the cross section is evaluated.

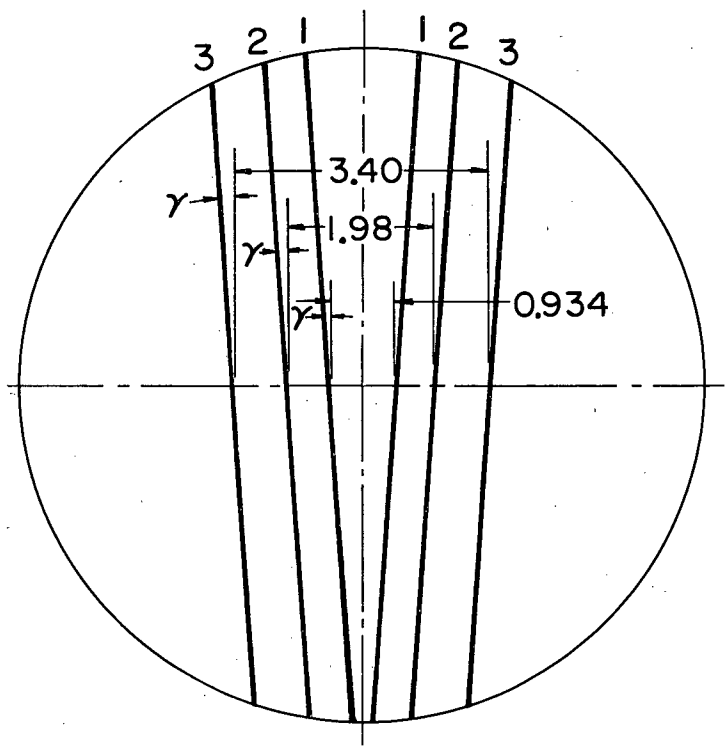

MU-24606

Fig. 9. Location of the planes defining the vertical boundaries of the five scanning regions. The lines also represent the limits by which frames were classified according to the amount of background. Type-1 frames are those for which obscuring background is contained within the pair of lines labeled 1. Similarly, type-2 and type-3 frames have background contained within lines 2 and 3, respectively. This classification is explained in Sec. VIII. The angle γ is 4 deg.

Table III. Table of scanner efficiencies

Scanner	Region 1	2	3	4	5
1	0.8889	0.8125	0.8889	0.8615	0.9435
2	0.7000	0.7500	0.8579	0.8475	0.9185
3	0.8000	0.7646	0.8511	0.7563	0.8862
4	0.7187	0.8182	0.8483	0.8582	0.9311
5	0.9655	0.9000	0.9487	0.9760	0.9825
6	0.9062	0.8000	0.9672	0.9626	0.9771
7	0.8000	0.7600	0.9163	0.8681	0.9324

B. Measuring

The events found by the scanners were measured on a device called OSCAR. The film was projected one view at a time upon a ground-glass screen. An operator moved a set of crosshairs to the desired points of the image and the coordinates were read out by an IBM card punch. The method of reconstructing the event is given in the following section.

IV. EVENT RECONSTRUCTION

A. Variables Measured

Measurements are made on the events to determine the following:

a. range of the π

b. angle of the π with respect to the beam

c. muon range

d. angle between the μ and the π

e. location of the event in the chamber.

Items a and b are used to calculate the kinematics of the photoproduction. The third item is used to determine the density of the liquid hydrogen from range-energy relations. The last two are used to calculate the probability of seeing and identifying an event.

B. Method for Reconstruction from Two-Dimensional Views

In the following, unprimed symbols pertain to the top lens or view 1, and primed symbols to the bottom lens or view 2, with "top" and "bottom" deriving from the physical orientation of the two camera lenses. The film is assumed parallel to the bubble-chamber windows. No optical corrections are made in the x and z coordinates but a thin window correction is made to the y coordinate, as will be explained.

Both windows have four crosses etched on them, forming the corners of a square with dimensions 5.08 by 5.08 cm^2. The eight crosses or fiducials on the two windows were aligned so that they formed a rectangular parallelepiped 5.45 cm thick. One of the fiducials on the camera window is used as the origin of coordinates and is denoted by F in Fig. 10. The z-axis is parallel to the beam; the y-axis is perpendicular to the windows and points away from the camera.

An arbitrary point in the chamber denoted by P(x, y, z) has coordinates x_1, z_1 and x_1', z_1' in views 1 and 2 respectively at the measuring screen. The x, y, z are connected to the x_1, z_1 and x_1',

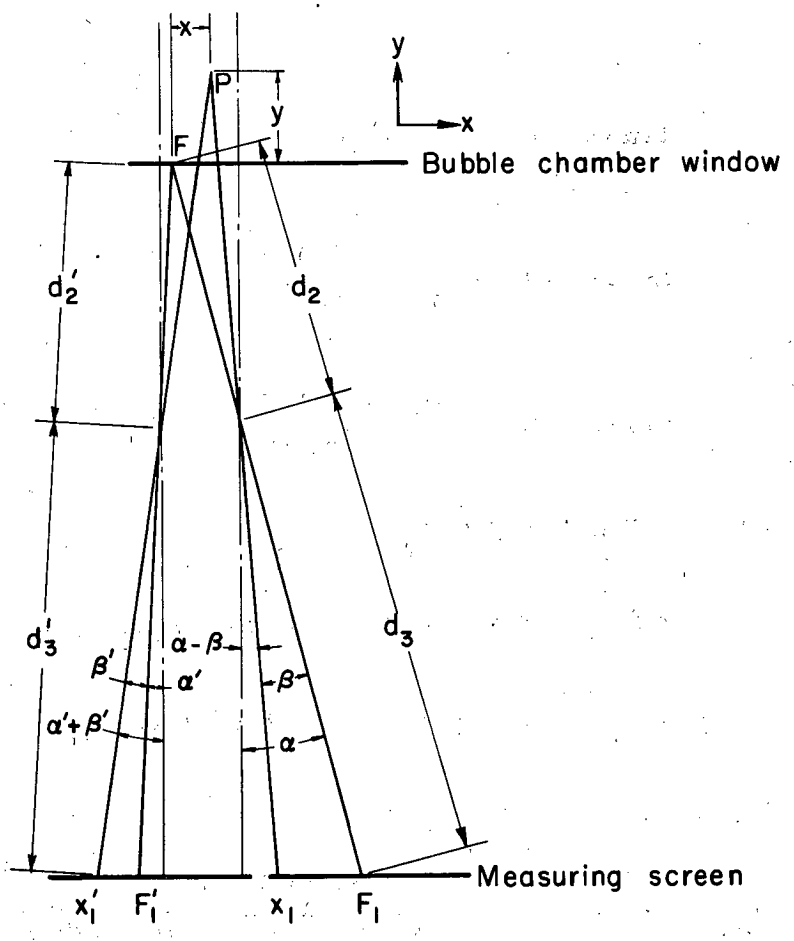

Fig. 10. Schematic of the light rays in the x-y plane. The point P at x, y, z in the chamber appears on the two views at the measuring screen at x_1, z_1 and x_1', z_1'.

z_1' through the tangents of the angles $(\alpha - \beta)$ and $(\alpha' + \beta')$ as follows:

$$\tan(\alpha - \beta) = \frac{x - d_2 \sin\alpha}{y + d_2 \cos\alpha} \tag{10}$$

$$\tan(\alpha - \beta) = \frac{x_1 - d_3 \sin\alpha}{d_3 \cos\alpha} \tag{11}$$

$$\tan(\alpha' + \beta') = \frac{x + d_2' \sin\alpha'}{y + d_2' \cos\alpha'} \tag{12}$$

$$\tan(\alpha' + \beta') = \frac{x_1' + d_3' \sin\alpha'}{d_3' \cos\alpha'} \,. \tag{13}$$

Eliminating the tangents gives

$$x\, d_3 \cos\alpha = y(x_1 - d_3 \sin\alpha) + x_1 d_2 \cos\alpha \tag{14}$$

$$x\, d_3' \cos\alpha' = y(x_1' + d_3' \sin\alpha') + x_1' d_2' \cos\alpha' \,. \tag{15}$$

Dividing Eq. (14) by Eq. (15) gives

$$y = \frac{(x_1 d_2 d_3' - x_1' d_2' d_3) \cos\alpha \cos\alpha'}{(x_1' + d_3' \sin\alpha')\, d_3 \cos\alpha - (x_1 - d_3 \sin\alpha) d_3' \cos\alpha'} \,. \tag{16}$$

Equation (14) is

$$x = \frac{y(x_1 - d_3 \sin\alpha) + x_1 d_2 \cos\alpha}{d_3 \cos\alpha} \,. \tag{17}$$

From Fig. 11, which shows the y-z plane, one can see that

$$z = \frac{z_1(y + d_2 \cos\alpha)}{d_3 \cos\alpha} - y \tan\gamma. \tag{18}$$

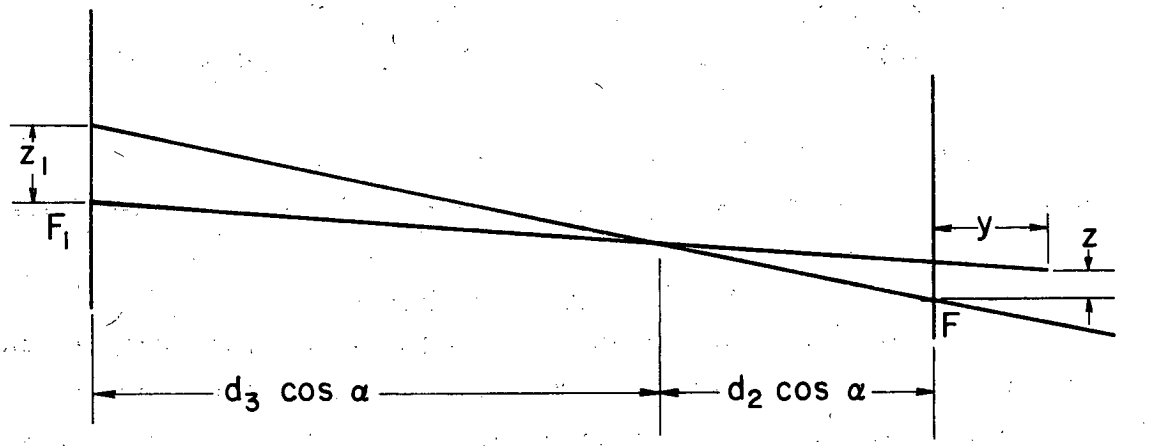

Fig. 11. Schematic of the light rays in the y-z plane.

The parameters a_1, d_2, d_3, a', d'_2, d'_3, and $\tan\gamma$ are determined from measurements on the fiducials etched on the windows. These parameters are listed in Table IV.

Table IV. Parameters for the measuring system

a = 10 deg 3 min	a' = 0 deg, 57 min
d_2 = 46.85 cm	d'_2 = 45.35 cm
d_3 = 37150 OSCAR units	d'_3 = 36099 OSCAR units
$\tan\gamma$ = 0.0798	
197 OSCAR units = 1 cm on the measuring screen	

C. Optical Corrections

The bubble-chamber and the vacuum-jacket windows, which can be seen in Fig. 8, cause distortion because the light rays are refracted. No significant distortion in the x-z plane is seen at the level of our measuring accuracy. Any such distortion would result in a difference between magnifications M_x and M_z in the x and z direction so that $M_x \leqslant M_z$. However the presence of mirrors in the measuring apparatus can also contribute to different magnifications. The actual difference measured is quite small and such that $M_z < M_x$, so we can not definitely say what factor causes the difference. The ratio of x-magnification to z-magnification is

$$\frac{M_x}{M_z} = 1.0053. \qquad (19)$$

Therefore no optical corrections are made in the x-z plane.

The correction in the y direction is made in the approximation of small angles. Using Snell's law and $\sin\theta \simeq \theta$, we have

$$y_{actual} = n y_{measured} ,$$

where n is a parameter that expresses an effective index of refraction. From measurements on the fiducials, we find n = 1.10; for comparison, the index of refraction for liquid hydrogen is 1.0974.

D. Event Analysis

The points measured on each event are:

a. two fiducials

b. origin of the muon

c. end point of the muon

d. four points along the muon track.

The fiducial measurements define the bubble-chamber coordinate system with respect to the measuring system. The range and location of the muon are calculated from items (b) and (c).

Item (d) is used to specify the pion track, which is characterized by the indeterminancy of the pion origin. In each view, a straight line is fitted to the four points measured. The parameters of these straight lines have errors, which are calculated in the usual manner associated with curve fitting. These errors are caused by measuring error, multiple scattering, and turbulence. In addition, the π-μ vertex coordinates have a measuring error. The two fitted lines are transformed into a single line in three-dimensional space by using Eqs. (16) to (18). The pion track is then described by the linear equations

$$y = b_1 + b_2 x, \tag{20}$$

$$z = b_3 + b_4 x, \tag{21}$$

and

$$x_{\pi\mu} = b_5, \tag{22}$$

where $x_{\pi\mu} = b_5$ is the x coordinate of the $\pi\mu$ vertex. The five parameters b_i have correlated errors which are expressed in a 5-by-5 error matrix h, the diagonal elements being the square of the errors on the b_i. A change of variables from b_i to b_i' requires the following transformation on the error matrix:

$$h' = (\Delta b')(h)(\overline{\Delta b'}), \tag{23}$$

where the matrix $(\Delta b')$ has elements

$$(\Delta b')_{ij} = \frac{\partial b_i'}{\partial b_j} \quad . \tag{24}$$

Below in this section, we define the boundaries of the beam in the bubble chamber. An event can originate anywhere within the bounds, but we assume that it begins at the center. Let the distance along the pion track from the beam boundary plane to the π-μ vertex be L, and the distance from the center line to the boundary be Δ. Then the track length is $R = L + \Delta$ with an uncertainty $\pm \Delta$. This uncertainty amounts to 0.5 Mev in the range of gamma-ray energies that we have, and the error matrix is modified accordingly.

From Eqs. (20) to (22), the cosine of the angle of emission from the beam is

$$\cos(\theta) = \frac{b_4}{(1 + b_2^2 + b_4^2)^{1/2}} \quad . \tag{25}$$

The pion kinetic energy, T_π, can be obtained from the pion range by using Eq. (49) of Sec. VI. From $\cos(\theta)$ and T_π, the photon energy, E_γ, can be calculated. Each change of variables from the $b_i \rightarrow (R_\pi, \theta) \rightarrow (T_\pi, \theta) \rightarrow (E_\gamma, \theta)$ requires a transformation of the error matrix according to Eq. (23).

The diagonal elements of the matrix representing the variables (E_γ, θ) are the square of the errors on E_γ and θ, and represent the experimental resolution. This amounts to $\Delta E_\gamma \sim 1$ Mev and $\Delta\theta \sim 0.03$ rad for three measurements per event.

E. Magnitude of the Errors

The root mean square (rms) measuring error on well-defined points is

$$\Delta x = 4.1 \text{ OSCAR units} \tag{26}$$

and

$$\Delta z = 4.5 \text{ OSCAR units.} \tag{27}$$

This corresponds to a standard deviation of 0.03 cm in any distance in the bubble chamber. The rms error in measuring actual tracks is 0.04 cm. The difference is attributed to the uncertainty caused by background and gives a measure of the increase in measuring error due to background.

The error analysis can be checked. If any discrepancy exists, it should be reflected most strongly in the angular errors because angles are the more difficult parameter to measure. The actual standard deviation of the angular measurements is $\Delta(\cos\theta) = 0.023$, where $\Delta(\cos\theta)$ is the average of the standard deviations of three measurements on each of eight events. The average angular error calculated from the error matrix, which expresses the angular errors in terms of known measuring errors, is $\delta(\cos\theta) = 0.021$. The difference between $\Delta(\cos\theta)$ and $\delta(\cos\theta)$ is not considered large enough to suspect that some unknown mechanism is affecting the measurements.

F. Beam Orientation

The orientation and location of the beam in the bubble chamber was determined by taking a roll of film with low beam intensity and with chamber conditions such that ionization by electrons would cause bubbles. The beam was then defined by the locations of the origins of 97 electron-positron pairs.

The slope in the y direction is -0.0663 and in the x direction, -0.00199. This corresponds to a deviation from a line parallel to the coordinate axis of 3 mm over the length of the chamber and is considered negligible since most of it is in the y direction. The events are distributed parabolically in the x and y direction and the intensities are well-fitted by

$$I_x = -6.65 + 5.17x - x^2 \qquad (28)$$

and

$$I_y = -6.82 + 5.47x - x^2. \qquad (29)$$

The boundaries of the beam are taken to be the zeroes of these distributions. Thus the extent of the beam is overestimated because measuring errors smear the distribution out. Figure 12 shows the cross section of the beam relative to the coordinate system. The two parabolic curves adjacent to the beam represent the intensity distributions I_x and I_z.

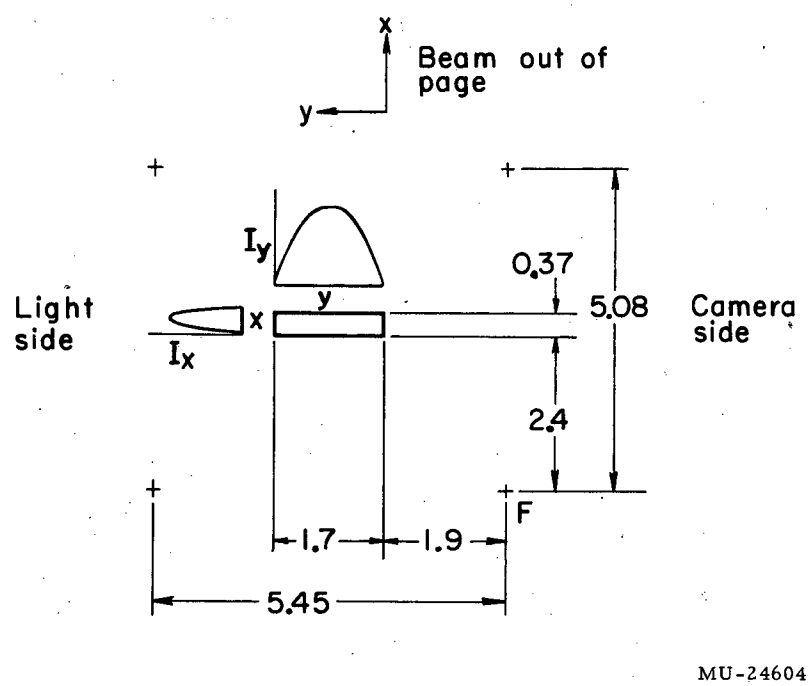

Fig. 12. Position of the beam in the chamber. The curves I_x and I_y represent the distribution of the beam intensity in the x and y directions. The cross, F, is the origin-of-coordinate fiducial.

V. CHAMBER EFFICIENCY

A. Qualitative Explanation

The chamber had a certain efficiency for producing a visible track for a pion of some range and angle. Figure 13a, b, and c, show three cases where this is manifest. In Fig. 13a, the vertex is obscured by the cell that was used to measure vapor pressure. In Fig. 13b, there is no method by which the pion can be distinguished from the muon. Finally in Fig. 13c it is doubtful whether the track represents π-μ decay, or a proton which scattered slightly. Each of these events could have occurred in an unambiguous configuration with equal probability. Therefore for an event with certain range and angle, there will be an efficiency factor, the inverse of which is the number of pions created for each pion seen.

B. Formulation of the Efficiency

In principle, the possible locus of the π-μ vertex is a right circular cylinder of altitude 2B and radius $R\sin\theta$ for an event of range R and polar angle θ, where B is the radius of the chamber. The efficiency of the chamber for this particular event is calculated by determining the amount of the cylindrical surface visible to a scanner, that is, the partial surface not obscured by the chamber walls or the vapor-pressure cell. The probability of distinguishing an event at a particular locus on the partial surface is not unity, because in some cases the muon may go into the beam as was seen in Fig. 13b or may be nearly parallel to the π track as in Fig. 13c.

Therefore in calculating the area of the partial surface, each locus must be weighted according to how much of the possible orientation of the μ around the π would give rise to a track that is unambiguously an event.

The chamber is a right circular cylinder of radius B = 4.5 cm. The beam area is defined by two slightly diverging planes perpendicular to the window. The shape of the vapor-pressure cell is irregular, although for calculation purposes it was assumed to be a cylindrical

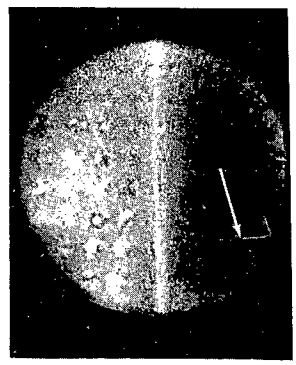

(a)

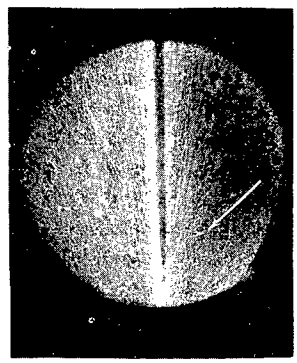

(b)

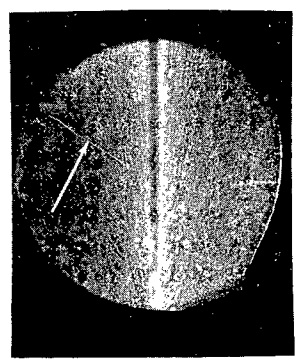

(c)

ZN-2978

Fig. 13. (a) A π-μ decay in which the π-μ vertex is obscured by the vapor-pressure cell. All events with vertices outside the cell boundary and other geometrical boundaries were excluded. (b) A π-μ decay in which the muon decays into the beam. There is no way to distinguish the pion from the muon, and all such events were excluded. (c) A track that may be a π-μ decay or a proton-proton scatter. The distributions of measured π-μ angles showed that for parallel or anti-parallel π-μ tracks with less than a 12-deg angle, the events were difficult to see and measure.

surface. The disposition of the geometry can be seen in Fig. 14. The dimensions were determined by projecting the muon origins and end-points on the x-y and x-z planes.

In the calculation, it is assumed that the pion is produced mid-way between the two diverging planes defining the beam area, but not necessarily midway between the bubble chamber windows. For a given event, the locus of possible pion origins is a line parallel to the z-axis, and it is equally possible for a pion to be produced at any point z on this line at any azimuthal angle ϕ about this line. The calculation is to integrate the possibility of seeing an event at some z and ϕ over all possible z and ϕ.

First the calculation is made for events that could have the muon go into the beam. Figure 15a shows schematically the orientation of a typical event relative to the boundary planes A and B defining the beam. The dashed pion track represents the portion obscured to the scanner. Figure 15b shows the event on projection in the x-y plane with azimuthal angle ϕ so that the muon is visible for all possible orientations. Figure 15c shows the same event with azimuthal angle ϕ so that part of the muon locus lies in the beam.

In Fig. 14b, the fraction of muon locus visible is

$$P_1(\phi) = 1 - \frac{\omega_p + \omega_a}{4\pi} \quad . \tag{30}$$

The ω_p and ω_a are the solid angles to be excluded for the muon either parallel (ω_p) or antiparallel (ω_a) to the pion track. In Fig. 15c the fraction of visible locus is

$$P_2(\phi) = \frac{1 + \cos\alpha}{2} - \frac{\omega_p + \omega_a}{4\pi} \quad . \tag{31}$$

As the angle increases, the probability becomes

$$P_3(\phi) = \frac{1 + \cos\alpha}{2} - \frac{\omega_p}{4\pi} \quad . \tag{32}$$

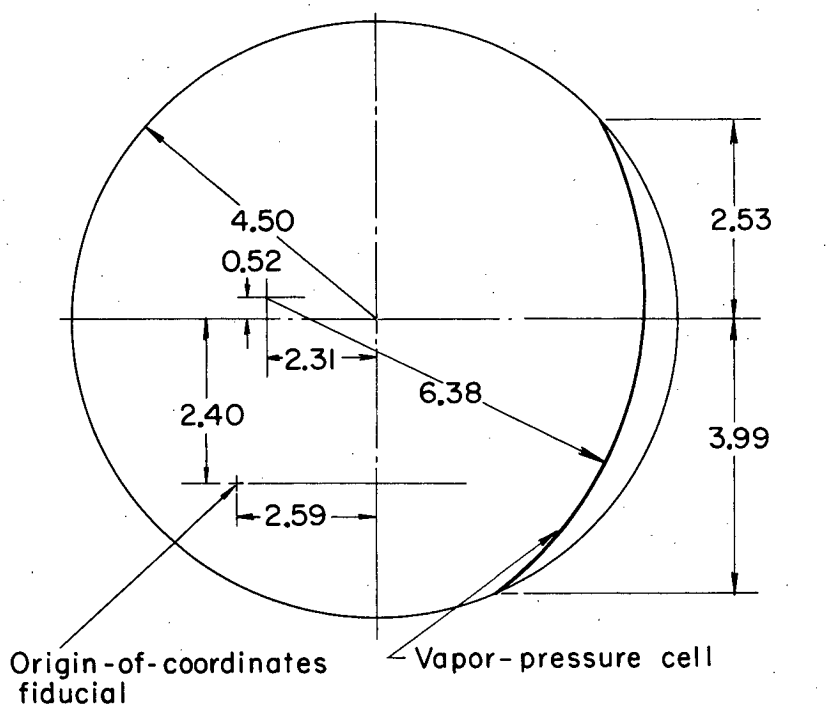

Fig. 14. Disposition of the chamber geometry. Dimensions are in centimeters.

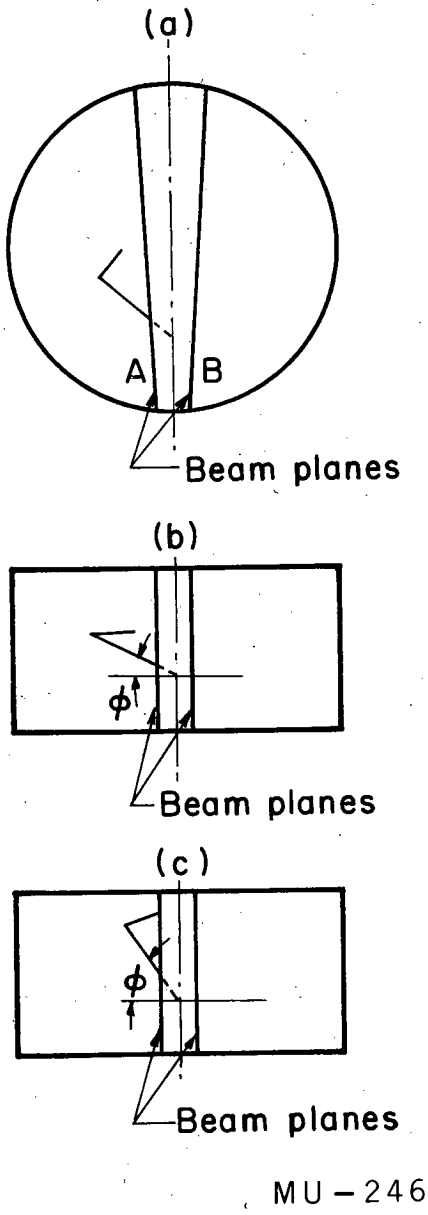

Fig. 15. Various orientations of an event with respect to the beam. (a) Top view of the chamber with the beam defined by planes A and B. Dashed portion of the pion track represents the part obscured. (b) Side view with all orientations of the muon visible. (c) Azimuthal angle ϕ has increased so that only a certain fraction of the muon orientations are visible.

In $P_3(\phi)$, the factor ω_a is missing because ϕ is large enough so that the $(1 + \cos\alpha)/2$ effectively excludes the portion of the solid angle containing ω_a. A small approximation has been made, which nearly balances out when the angle ϕ is integrated over. This is the complete exclusion of ω_a at the angle ϕ_h when the intersection of the pion track and the muon locus strikes the plane defining the beam.

The weights $P(\phi)$ are integrated over the angle ϕ at some point z in the chamber:

$$P(z) = \int_{\phi_a}^{\phi_o} P_1(\phi)d\phi + \int_{\phi_o}^{\phi_h} P_2(\phi)d\phi + \int_{\phi_h}^{\phi_e} P_3(\phi)d\phi. \qquad (33)$$

The lower limit in the first integral may not be zero if z is near the extremes of the chamber, because there are values of z such that at $\phi \leq \phi_a$, the muon origin strikes the cylindrical wall of the bubble chamber. The muon tracks are almost always $\leq$ 1.5 cm, and so if the visible pion track is greater than 2 cm, then the event is considered unambiguous even if the muon goes in to the beam. For such cases ϕ_o and ϕ_h are set to the limit when less than 2 cm is visible.

Of course ϕ_a may be greater than ϕ_o or ϕ_h, so that either of the first two integrals may be missing for some $P(z)$. The upper limit ϕ_e is the azimuthal angle when the muon origin strikes the beam plane or the bubble chamber window, which ever happens first.

The function $\cos\alpha$ at some angle ϕ is given by

$$\cos\alpha = \frac{R_\pi \sin\theta\cos\phi - (d + ez)}{R_\mu}. \qquad (34)$$

Subscripts on the R's denote pion and muon ranges respectively. The factor $d + ez$ is half the separation of the diverging beam planes at z.

The integral $P_B(z)$ over $0 \leq \phi \leq \phi_{e_2}$ is of the form

$$P_B(z) = (\phi_o - \phi_a)\left(1 - \frac{\omega_p + \omega_a}{4\pi}\right) + \frac{R_\pi \sin\theta}{2 R_\mu} (\sin\phi_h - \sin\phi_o)$$

$$+\left[\frac{1}{2} - \left(\frac{d + ez}{2 R_\mu} + \frac{\omega_p + \omega_a}{4\pi}\right)\right] (\phi_h - \phi_o) + \frac{R_\pi \sin\theta}{2 R_\mu} (\sin\phi_e - \sin\phi_h)$$

$$+\left[\frac{1}{2} - \frac{d + ez}{2 R_\mu} + \frac{\omega_p}{4\pi}\right] (\phi_{e_2} - \phi_h) . \qquad (35)$$

Another similar integral over $-\phi$ must be calculated, since the pion is not produced midway between the windows. This creates two upper limits, ϕ_{e_2} and ϕ_{e_1}. If the muon can not strike the beam because the pion track is too large, then we have $\phi_o = \phi_h = \phi_e$ and only the bubble-chamber walls and windows can obscure the track.

Because ϕ_o, ϕ_{e_2}, ϕ_{e_1}, and ϕ_a depend nonlinearly on z, the subsequent integral of $P_B(z)$ over z is done numberically. The subscript B on P_B denotes the efficiency factor calculated from the beam geometry. Similarly there is a factor P_{vp} because of the vapor pressure cell geometry.

The chamber is large enough that if an event is long enough to be obscured by the vapor-pressure cell at any z, the muon can not decay into the beam area. Therefore the geometrical efficiency factor of the vapor-pressure cell may be calculated without consideration of the geometry of the beam area.

Figure 14 shows the position of the vapor-pressure cell. The radius of the cell is R_{vp}, where

$$R_{vp}^2 = (x - x')^2 + (z - z')^2 . \qquad (36)$$

Here x', z' are the coordinates of the center of curvature of the cell boundary. The angle ψ_o is the azimuthal angle at which the muon origin is obscured by the vapor pressure cell. The equation for ψ_o is

$$\cos\psi_o = \left[\left[R_{vp}^2 - (z - z')^2\right]^{1/2} + x'\right] \Big/ R \sin\theta . \qquad (37)$$

At some z, the amount of azimuthal angle for which the event is visible is

$$P_{vp}(z) = \phi_{max\ 1} - \psi_o + \phi_{max\ 2} - \psi_o \tag{38}$$

for $\psi_o \leq \phi_{max\ 1} \leq \phi_{max\ 2}$,

$$P_{vp}(z) = \phi_{max\ 2} - \psi_o \tag{39}$$

for $\phi_{max\ 1} \leq \psi_o \leq \phi_{max\ 2}$, and

$$P_{vp}(z) = 0, \tag{40}$$

for $\phi_{max\ 1} \leq \phi_{max\ 2} \leq \psi_o$.

The $\phi_{max\ 1}$ and $\phi_{max\ 2}$ are the angles at which the muon origin strikes the lower and upper windows. At extreme values of z, the muon origin may strike the cylindrical walls of the chamber, and ψ_o should be replaced by ϕ_a for $\phi_a \geq \psi_o$.

To determine the solid angle over which the track would be visible, we integrate the weights $P_{vp}(z)$ numerically over z:

$$P_{vp} = \int_{-B}^{B} P_{vp}(z)\, dz. \tag{41}$$

The total solid angle available to the track is then

$$P = P_{vp} + P_B \tag{42}$$

if the track hits vp cell; if the track doesn't hit vp cell, it is

$$P = 2P_B. \tag{43}$$

Events that had the largest geometrical efficiency were those produced by photons of 158- to 162-Mev energy, where the pion came out at reight angles to the beam. These types had efficiencies around 80%, whereas the majority of the events with different angles or ranges had efficiencies of 30 to 50%.

C. Limits on the π-μ Angle

The angles ω_p and ω_a, at which the tracks of the π and the μ were considered so nearly parallel or antiparallel that they were not identifiable, were determined by looking at the distribution of the cosines of the angles between the π and the μ for 1700 events.

When the μ is nearly parallel to the π (large opening angle), the vertex is exceedingly difficult to measure. Any error in locating the vertex by the measurer tends to increase the calculated angle between the π and μ. Therefore, it was observed that near $\cos \theta_{\pi\mu} = 1.0$, the distribution will not fall off as it should. Accordingly, we assume that the angles of exclusion, ω_p and ω_a, are nearly the same and look at the distribution near $\cos \theta_{\pi\mu} = 1.0$ where the vertex is well-defined.

There were 386 events with an angle in the range $\cos \theta = -1.0$ to -0.52, and 405 in the range $\cos \theta = -0.52$ to -0.04. Therefore the fractional difference was $368/405 = 0.953$, corresponding to a range of angles, $\cos \theta = -1.0$ to -0.977, not being seen by the scanners. Thus we set the limit on the $\pi - \mu$ angle at 12 deg and we have

$$\omega_a = \omega_p = 2\pi \times 0.023. \tag{44}$$

VI. RANGE-ENERGY RELATIONS

A. Proton Ranges in Hydrogen

Range-energy relations were used to obtain the kinetic energy of the pions from the observed range and to calculate the density of the liquid hydrogen from the observed range of the muons. The range-energy calculations are given in some detail because the results obtained differ from published data. Ranges of protons in gaseous hydrogen were obtained by integrating the stopping cross section of Bohr over energy as discussed by Whaling.[13] The results were around 2% less than those given by Whaling.

The region of calculation was for velocities up to 0.45c, and a stopping cross section that contains relativistic modifications was used, such as that found in Aron's thesis:[14]

$$\sigma_{\text{stopping}} = \frac{4\pi e^4}{m_o \beta^2} \left\{ \ell n \frac{2m_o \beta^2}{I(1-\beta^2)} - \beta^2 \right\}, \tag{45}$$

where e is the electron charge, m_o is the electron mass, β is the particle velocity in units of c, and I = 16.1 ev is the ionization potential of hydrogen gas.[15]

This leads to an energy loss per cm of

$$\frac{dT}{dR} = \frac{0.30489}{\beta^2} \left\{ \ell n \left[63{,}476 \left(\frac{\beta^2}{1-\beta^2} \right) \right] - \beta^2 \right\} \frac{\text{Mev-cm}^2}{\text{gm}}, \tag{46}$$

where T is the kinetic energy, and R is the range.

It may not be valid to use the ionization potential of gaseous hydrogen for the liquid state, but no experimental data exist for the liquid-state potential.

Bohr's theory is not valid as the incident-particle velocity approaches the electron orbit velocity. In the calculation, some experimentally determined range is chosen at a low energy and integrated from that point:

$$R(T) = R(T_o) + \int_{T_o}^{T} \frac{dT}{dT/dR} \quad . \tag{47}$$

The calculation was done with an IBM 650; the program was checked by duplicating Aron's results. Table V gives the ranges versus energy.

The data were corrected for use with pions by the relationships

$$R(T_\pi) = \frac{M_\pi}{M_P} \; R_P(T') \; ; \quad T' = \frac{M_P}{M_\pi} \; T_\pi \quad . \tag{48}$$

Over the short range of 1 to 10 Mev, the following functional dependence is valid:

$$\ell n \; T_\pi = 3.056 + 0.548 \; \ell n \; R_\pi ; \; R_\pi \text{ in gm/cm}^2. \tag{49}$$

B. Liquid-Hydrogen Density

1. Density

The density ρ of the liquid hydrogen was determined by substituting the average muon range $\overline{R}$ and muon energy into a range-energy relationship similar to Eq. (49). Muons used for determining the average muon range were selected from 2000 events. The following requirements were made for each selected muon:

1. dip angle less than 30 deg.
2. end or origin no closer than 2.5 mm from any chamber boundary.
3. end or origin no closer than 2.0 cm from center of beam area
4. clean, sharp end-point and vertex
5. well-defined track.

A computer selected 300 muons on the basis of criteria 1, 2, and 3. Scanners then graded these for requirements 4 and 5. This left 67 muon tracks with which to obtain the range. The result was $\overline{R}$= 1.142 ± 0.009 cm with a standard deviation of the distribution being 0.074 cm. The distribution of events in Fig. 16 shows no reason to assume that there was any bias for short or long tracks.

Table V. Range of protons in hydrogen

Kinetic energy (Mev)	Range (gm/cm^2)
1	0.0008214
2	0.002787
3	0.005776
4	0.009728
5	0.01460
6	0.02038
7	0.02702
8	0.03452
9	0.04285
10	0.05201
11	0.06198
13	0.0830
15	0.1097
17	0.1382
19	0.1697
20	0.1866
25	0.2816
30	0.3941
35	0.5236
40	0.6694
45	0.8312
50	1.008
60	1.408
70	1.865
80	2.378
90	2.943
100	3.560

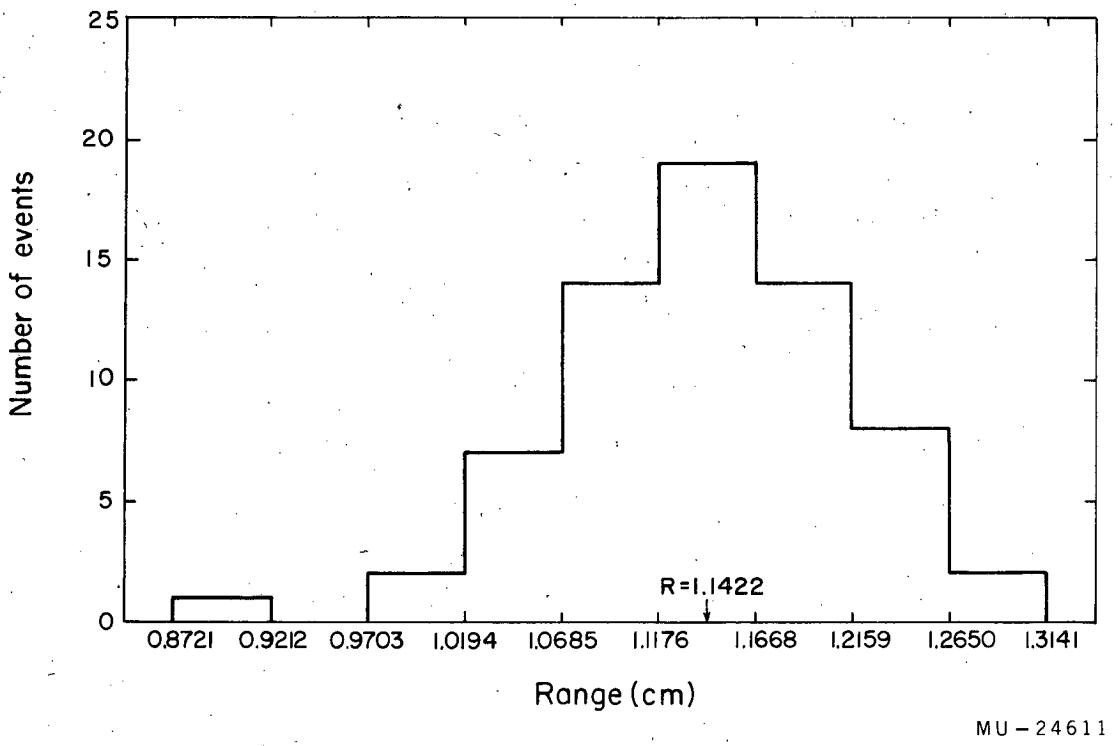

Fig. 16. Distribution of the ranges of 67 muons used to determine the average muon range for the density calculation. The average range measured was 1.142 cm.

The expected standard deviation of the distribution was calculated to check that the selection procedure did not affect the distribution and that there were no unknown errors contributing to the spread. It was assumed that the distribution was solely due to range straggling and measurement error.

The standard deviation, σ_r, of the actual ranges about the mean ranges because of straggling is derived by Evans.[16] Actually what is given is $d\sigma_r^2/dE$, and this must be integrated numerically over energy. For muons of 4.12-Mev energy and 0.055 gm/cm^3 hydrogen density, σ_r is 0.037 cm.

A track-length measuring error of $\sigma_m = 0.040$ cm gives a total standard deviation

$$\sigma^2 = (\sigma_r^2 + \sigma_m^2)^{1/2} = 0.056 \text{ cm.} \qquad (50)$$

Comparison with the actual standard deviation of 0.074 cm offers no basis for assuming that the selection procedure affected the distribution or that there were unsuspected errors operative.

The density was then calculated by using Eq. (49) modified for muons, and the following parameters:

$$M_\pi = 139.63 \pm 0.06 \text{ Mev}$$

$$M_\mu = 105.70 \pm 0.06 \text{ Mev}$$

$$E_\mu = 4.12 \pm 0.02 \text{ Mev}$$

$$\overline{R}_\mu = 1.142 \pm 0.009 \text{ cm.}$$

A density of 0.0552 ± 0.00065 gm/cm^3 was obtained as compared to 0.05863 gm/cm^3 obtained by Reed and Tripp for the 15-in. chamber.[12] Two percent of the discrepancy arises from the difference in muon ranges in the two chambers, because the 4-in. chamber hydrogen was warmer. The remaining 4% is due to the different range-energy data used by Reed and Tripp.

2. Number of targets per cm^2

The path length in hydrogen of photons that produce geometrically acceptable events is 9 cm. Thus the density in gm/cm^2 is

$$\rho = 9 \times 0.0552 \text{ gm/cm}^2 = 0.497 \text{ gm/cm}^2. \tag{51}$$

The number of targets per cm^2 is

$$\begin{aligned} N &= 0.497 \text{ gm/cm}^2 \times 1/1.008 \text{ gm/mole} \times 6.025 \times 10^{23}/\text{mole} \\ &= 0.297 \times 10^{24}/\text{cm}^2. \end{aligned} \tag{52}$$

VII. ANALYSIS OF THE SYNCHROTRON BEAM

In order to calculate a cross section, the number of photons of a given energy are needed. Because the photon spectrum is continuous, this number really has no significance. However, since it is convenient to think in terms of the number of incident photons, we consider that all photons with energy between the limits of $k \pm 1/2$ Mev have energy k. To obtain the "number" of photons of energy k, we determine the amount of energy, ΔE, incident upon the chamber due to photons of energy $k \pm 1/2$, and divide by k. Thus we have

$$N_k = \frac{\Delta E}{k} \quad . \tag{53}$$

The 1-Mev width of the bins corresponds to the energy resolution of the experiment.

A. Calibration of the Cornell Ion Chamber

The Cornell chamber was used to measure the beam incident on the chamber. The response, M, of the Cornell chamber is expressed as the ratio of the energy incident on the chamber to the charge collected, Q'.

$$M = \frac{\text{Energy}}{Q'} \tag{54}$$

The response of a chamber filled at 0°C and 760 mm pressure with k_{max} = 189.1 Mev (taken from Fig. 2 of Loeffler, Palfrey, and Tautfest[17]) is

$$M_{\text{Loeffler}} = (3.311 \pm 0.1015) \times 10^{18} \text{Mev/coul.} \tag{55}$$

The filling conditions are not known for the chamber used during our experiment, chamber A. Therefore we calibrated it against a chamber B which was filled at 29.4°C and 732.5 mm Hg with k_{max} = 189.1 Mev. The response of chamber B was

$$M_B = (3.742 \pm 0.1147) \times 10^{18} \text{ Mev/coul.} \tag{56}$$

The ratio between (B) and (A) is $M_B/M_A = 0.977 \pm 0.005$; therefore we have

$$M_A = (3.830 \pm 0.118) \times 10^{18} \text{ Mev/coul}, \tag{57}$$

where T and P are unknown, and $k_{max} = 189.1$.

The relationship M = Energy/Q' is used to normalize the intensity spectrum of the bremsstrahlung, since the incident energy is

$$\text{Energy} = A' \int_0^{k_{max}} k \frac{d\sigma}{dk} \, dk, \tag{58}$$

where $d\sigma/dk$ is the bremsstrahlung cross section, k_{max} is the peak photon energy, and A' is the normalization factor. Therefore we have

$$A' = \frac{Q'M}{\int_0^{k_{max}} k \frac{d\sigma}{dk} \, dk} . \tag{59}$$

The product $k \, d\sigma/dk$ is designated as the intensity spectrum.

B. Charge Collected by the Cornell Chamber

The charge, Q, was collected by the Cornell chamber in a beam that was modified by the lithium hydride. We determined that the ratio of the charge per synchrotron pulse with the LiH in and out of the beam was

$$R = 0.484 \pm 0.007. \tag{60}$$

Therefore the charge that would have been collected if the LiH had not been in the beam is

$$Q' = \frac{Q}{R} . \tag{61}$$

Note that Q' is used in Eq. (59) because the Cornell chamber calibration refers to an unmodified synchrotron beam. The normalization that is found using this adjusted charge Q' is for the spectrum incident on the LiH. This spectrum must be multiplied by the transmission of the photons through the LiH to obtain the spectrum at the bubble chamber; this is done at the end of this section.

In the following section, we show in the cross-section formula, Eq. (70), that the number of photons must be separated into the number for types 1, 2, and 3 pictures, corresponding to whether the obscuring background is contained within the sets of diverging planes 1, 2, or 3 of Fig. 9, of the next section. To do this we break up the total charge Q' into the charges Q'_1, Q'_2, and Q'_3 for types 1, 2, and 3 pictures in the following way:

$$Q'_i = \sum_{\substack{\text{rolls of} \\ \text{film } j}} (\text{No. of type-i pictures for roll j}) \times \begin{matrix}\text{charge per} \\ \text{pulse for} \\ \text{roll j}\end{matrix} , \tag{62}$$

where i = 1, 2, or 3 is the type of picture, and j = 1, 2, ··· 381 is the number of rolls of film.

C. Bremsstrahlung Intensity-Spectrum Integral

The integral of the energy spectrum is the remaining unknown term of Eq. (59) by which the intensity spectrum normalization is calculated.

1. Upper limit on peak photon energy

In order to evaluate the integral, the peak energy of the photons, k_{max}, must be known. This was determined by placing a pair spectrometer in the beam as shown in Fig. 17. A schematic of the spectrometer is shown in Fig. 18. If the members of an electron-positron pair enter either detectors 2 and 5 or 3 and 6, a coincidence is formed and registered. Because of the 60-deg geometry, the radius of curvature of a particle required to reach the nth detector is the same as the target-to-detector separation, ρ_n. If we neglect the square of the electron mass with respect to the square of the electron or positron momentum, the momentum of a gamma ray effecting a coincidence in one of the two channels 2, 5 or 3, 6 is

$$k = \frac{e}{c} H (\rho_2 + \rho_5) \text{ for channel 2, 5}$$

or (63)

$$k = \frac{e}{c} H (\rho_3 + \rho_6) \text{ for channel 3, 6.}$$

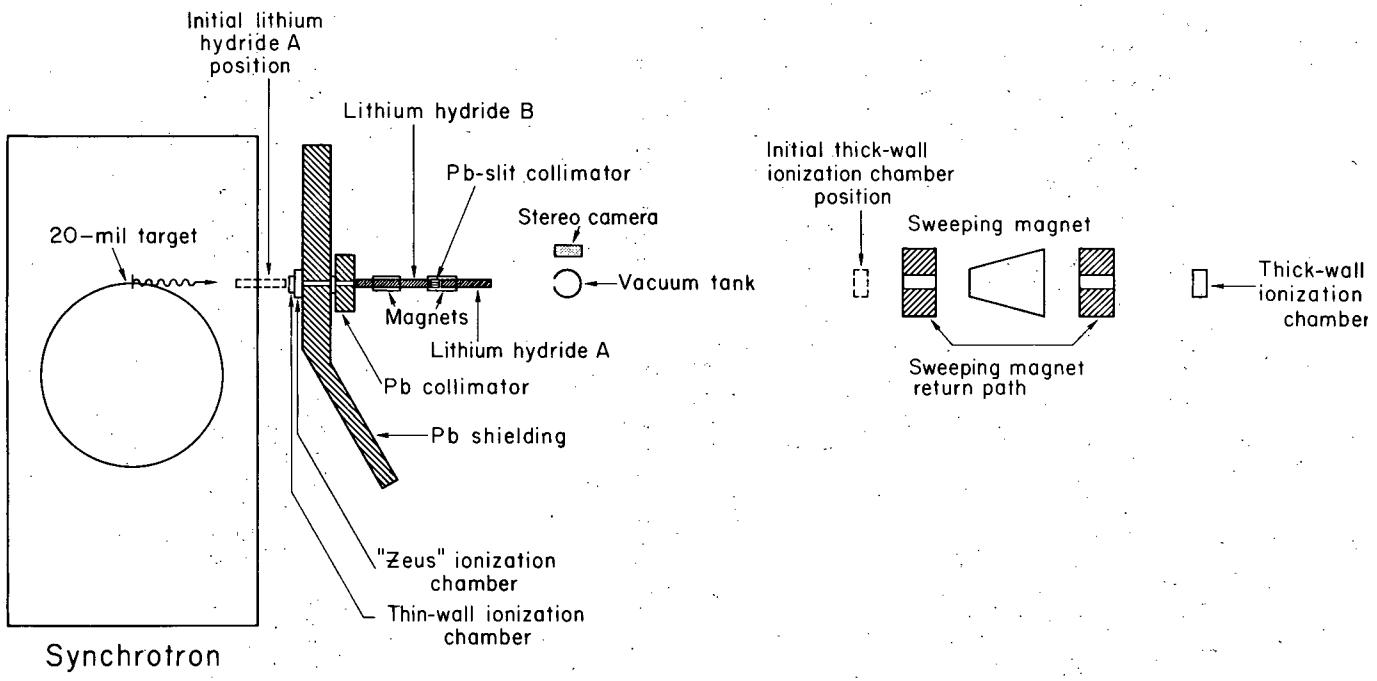

Fig. 17. Experimental setup for beam normalization. The bubble chamber was removed and just the vacuum tank was left in position. The tube of LiH, "A", has been moved from its initial position to behind the slit collimator. The Cornell ionization chamber has been moved to the far right and the pair spectrometer labeled "Sweeping magnet" has been inserted in the beam.

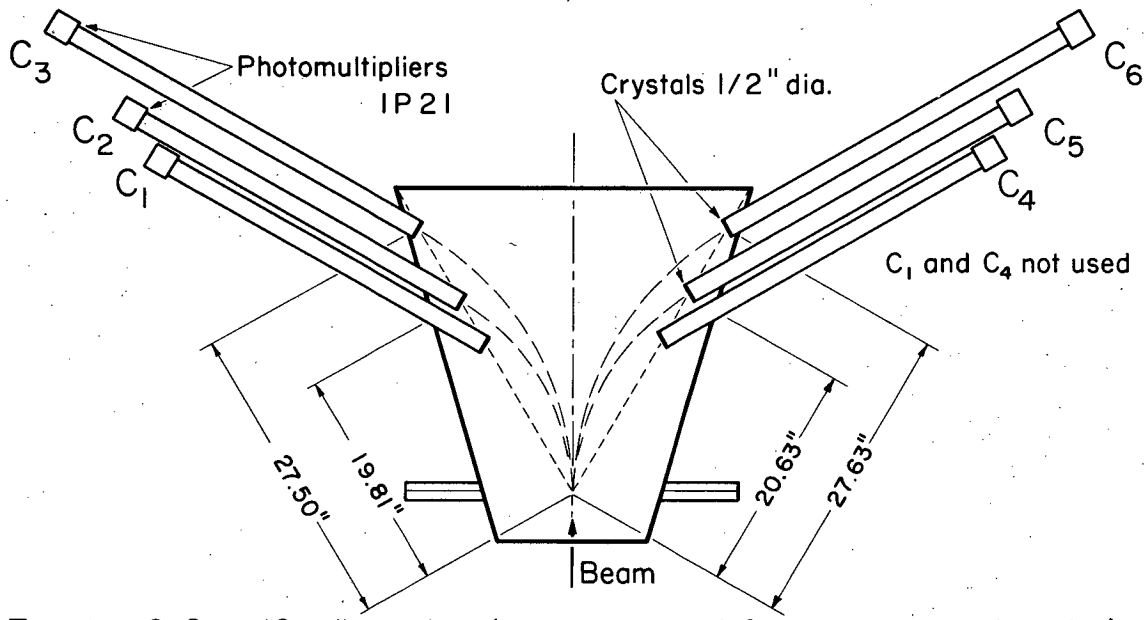

Fig. 18. Geometry of 60-deg pair-spectrometer pole tips, showing positions of the counters. Electron pairs produced in the thin Ta targets were detected in coincidence by counter pairs (2 + 5) and (3 + 6).

The peak energy is measured by increasing the pair-spectrometer field H until the count rate goes to zero. Figures 19 and 20 show the count rate versus magnetic field for channels 2, 5 and 3, 6, respectively. The magnetic field was measured by reading the voltage across a current shunt with a Leeds and Northrup potentiometer. The instrument was calibrated to the actual magnetic field by using magnetic-resonance methods with the result B(kgauss) = 0.0759 + 0.526 V (Mev). The abscissas of Figs. 19 and 20 are expressed in the magnet shunt voltage.

The curves in Figs. 19 and 20 are least-squares fitted to the experimental points. Table VI gives the results.

Table VI. Data for calculating the peak energy

Channel	Magnet shunt voltage at cutoff	χ^2	Degrees of freedom	Prob. of exceeding χ^2 (%)	Peak energy
3, 6	10.88 ± 0.26	0.37	2	20	191.0 ± 6.92
2, 5	11.69 ± 0.43	0.43	2	70	188.3 ± 4.37

The weighted average of channels 2, 5 and 3, 6 is

$$k_{max} = 189.1 \pm 3.7 \text{ Mev.} \tag{64}$$

The error is one standard deviation, if we assume a Gaussian distribution for the measurement.

2. Intensity Spectrum

a. Uncorrected bremsstrahlung cross section. The method of integrating the energy spectrum

$$I = \int_0^{k_{max}} k \frac{d\sigma}{dk} dk \tag{65}$$

is described here. Unfortunately, instead of using existing integrated cross sections for circular collimators, we have to integrate the bremsstrahlung cross section over angles of photon emission because

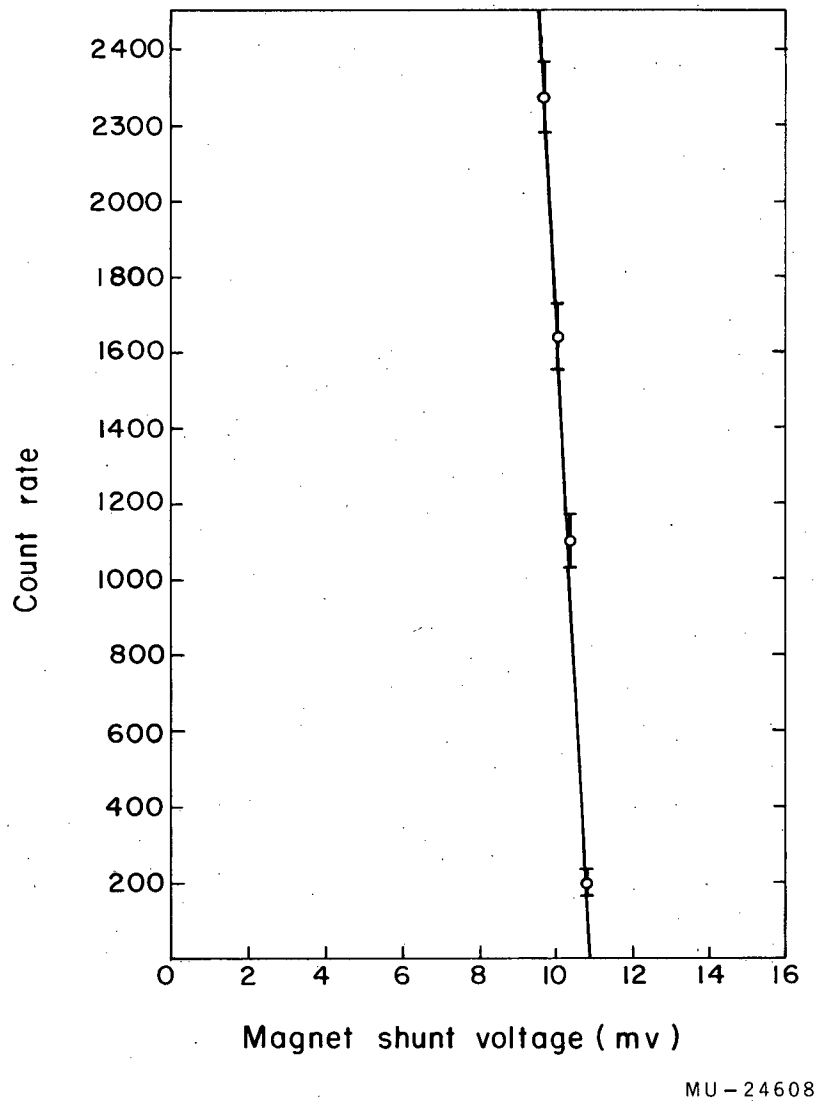

Fig. 19. Count rate per unit beam versus magnet-shunt voltage for channel 3, 6. Zero count rate is at 10.88 mv corresponding to 191.0-Mev peak energy.

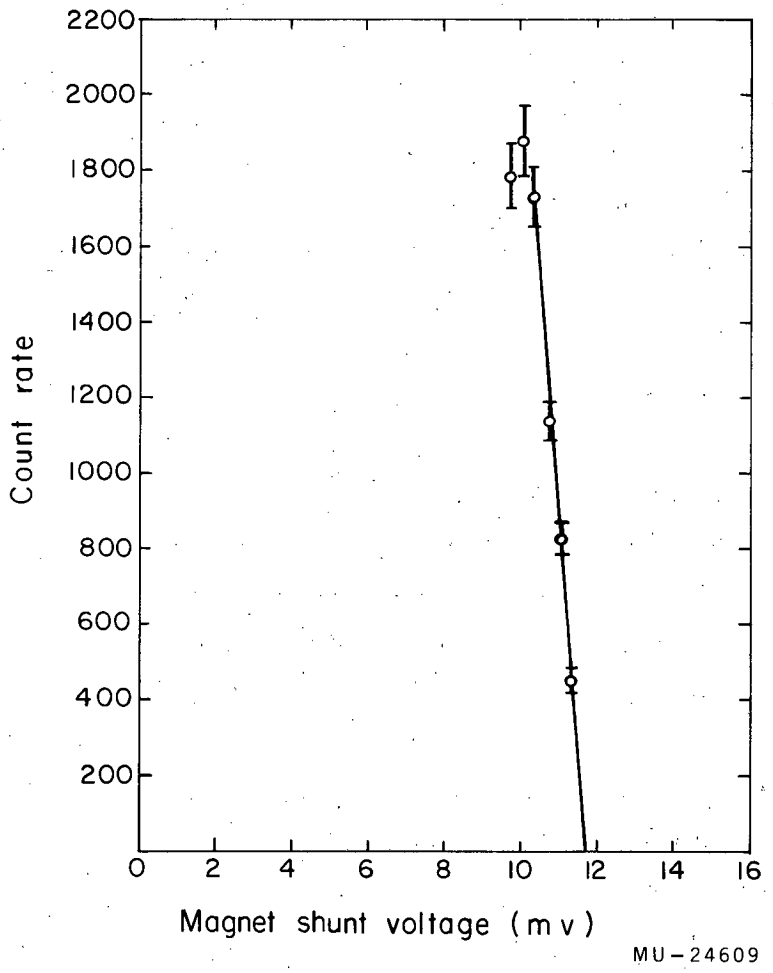

Fig. 20. Count rate per unit beam versus magnet shunt voltage for channel 2, 5. Zero count rate is at 11.69 mv, corresponding to a 188.3-Mev peak.

we used a rectangular shaped collimator. To accomplish this, we have written an IBM 709 program which numerically integrates the cross section over angles of emission and energy, taking into account synchrotron target corrections for multiple scattering and absorption of radiating electrons, and for photon absorption. The details of the program will be given elsewhere.

The bremsstrahlung cross section has been evaluated most recently by Olsen and Maximon, who used Sommerfeld-Maue-type wave functions in a screened Coulomb field.[18,19] They show that these wave functions are correct to $(Z/137)^2/k_{max}\ \ell n\ k_{max}$, which is 1 to 2% in this experiment. This is a great improvement over the bremsstrahlung cross section calculated in the Born approximation, which is 10% too high for heavy elements.

The Sommerfeld-Maue wave function, ψ, is obtained by considering it to be the relativistic generalization of the known solution, ψ_s, of the Schroedinger equation with a Coulomb potential. One may obtain an explicit ψ by assuming that the wave function $\psi = (1 + \Omega)\psi_s$ satisfies the approximate relativistic wave equation in which all terms in $(1/r)^3$ or higher order are dropped. The Ω is an operator and the derivation is given by Olsen and Maximon.

b. Screening correction. A correction to this cross section must be made to account for the screening of the nuclear Coulomb field by the orbital electrons. The amount of screening used depends upon a parameter proportional to $(1 + k_{max}^2\ \theta^2)^{-1}$, where θ is the angle of photon emission. For large photon energy or angle of emission, the radiating electron passes close to the nucleus and there is no screening. For small photon energy and angle of emission, the screening is at a maximum. For values between these extremes, the screening depends upon the magnitudes of the photon energy and angle. Therefore as the cross section is integrated over emission angles for various energies, it is multiplied by the proper screening factor, which depends upon the values of angle and energy.

c. Corrections for synchrotron target. The multiple scattering of the electrons in the synchrotron target alters the angular distribution of the photons that are able to pass through the collimator. We use a procedure suggested by Hisdal.[20] Using the multiple-scattering theory of Molière, we calculate the probability that the electron scatters by an angle θ before it radiates. The photon emission angle must be near θ in order for the photon to clear the collimator. Therefore we integrate the bremsstrahlung cross section over the range of angles around θ for which the photon can clear the collimator, and then multiply this result by the probability that the electron scattered through the angle θ in the first place.

This product is the cross section for an electron scattered by an angle θ to produce a photon that will clear the collimator. This must be integrated over all θ, since electrons may scatter over all θ before radiating. This procedure is done for successive values of photon energy k.

Further corrections required because of the target are:

a. attenuation of the primary electron beam because of radiation of high-energy photons
b. absorption of photons
c. energy loss by electrons because of ionization and low-energy radiation
d. increased path length.

We have treated these according to the method of Wilson.[21] To first order, these corrections are dependent only upon photon energy and are expressed in terms of a multiplicative factor, which is the fraction of photons coming out of the target versus the total number that would have been produced if the target thickness had no effect.

3. Value of the integral

The corrected intensity spectrum is shown as curve III in Fig. 21. When this curve is normalized so that the area under the curve is equal to the energy incident on the chamber, the ordinates are the product of the energy k times the "number" of photons per Mev at that energy. The area of the unnormalized intensity

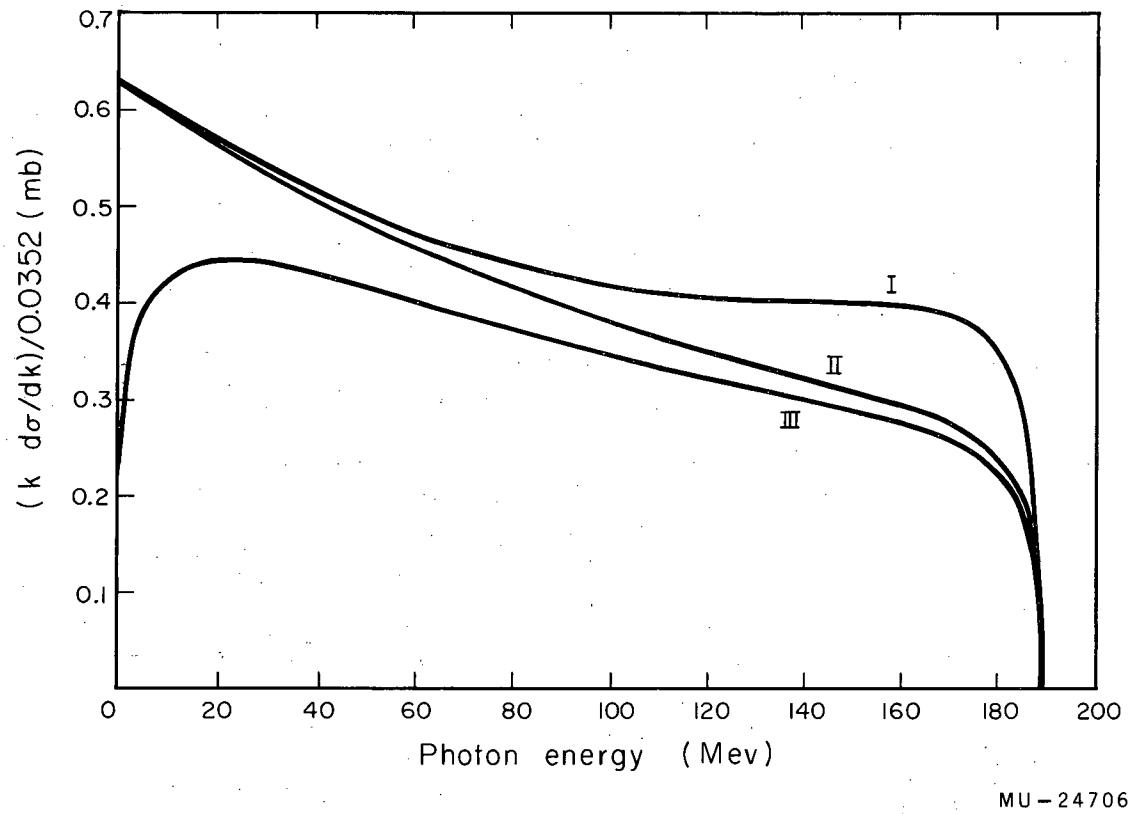

Fig. 21. Bremsstrahlung intensity spectra. I. Schiff spectrum with no target correction (normalized to Curve II at k = 0); II. Calculated spectrum with multiple-scattering correction only; III. Calculated spectrum with multiple-scattering and other thick-target corrections. All three spectra represent the beam as it leaves the synchrotron.

spectrum III is $I = 0.653 \times 10^{-3}$ Mev. Curve II of Fig. 21 is the intensity spectrum with the multiple-scattering corrections only. Curve I is the Schiff spectrum normalized to curve III at zero energy. This curve is given as a reference to previous calculations of the spectrum.

We now have the necessary information to calculate the beam normalization according to Eq. (59). In Eq. (62) the charge Q_i' has been calculated for the three types of film, i = 1, 2, 3. Therefore we obtain three normalizations, A_i, one for each film type. They are:

$$A_1' = \frac{Q_1' M}{I} = 45.98 \times 10^9$$

$$A_2' = \frac{Q_2' M}{I} = 28.96 \times 10^9 \qquad (66)$$

$$A_3' = \frac{Q_3' M}{I} = 2.704 \times 10^9.$$

The primes on the A's mean that this normalization is for the beam as it leaves the synchrotron. The effect of the LiH has to be considered.

4. Transmission through the Lithium Hydride

By using the pair spectrometer discussed in the peak-energy paragraph, we determined the transmission of the photons through the LiH versus photon energy. Figure 22 is a plot of this data. The best fit is a straight line representing a transmission of $T(k) = 0.5116 \pm 0.0055$, which is independent of photon energy. The probability of exceeding χ^2 was 36%.

The data were taken by recording the count rates of channels 2, 5 and 3, 6 with the LiH in and out for various field strengths in the spectrometer. The ratios of these count rates, corrected for background and accidentals, are the transmissions for photons of energies corresponding to the channel energies for the various field strengths. Thus transmissions at two energies were taken at each magnet setting.

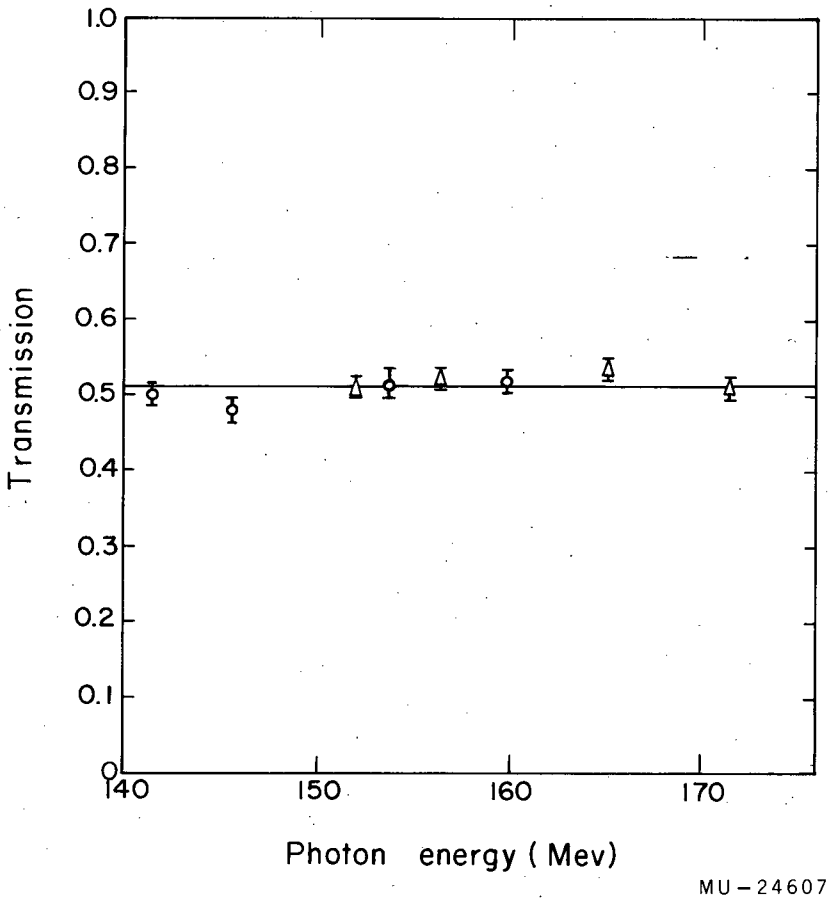

Fig. 22. Transmission of the photon beam through the LiH beam "hardener." For this range of energies, the transmission is independent of energy and equals 0.5116 ± 0.0055.

The relationship between the channel energies and the field strengths is given in the peak-energy paragraph.

D. Normalized Intensity Spectrum

The normalized intensity spectrum at the bubble chamber can now be calculated. The normalization factors for the three types of film are

$$A_1 = T\,A_1' = 23.53 \times 10^9$$

$$A_2 = T\,A_2' = 14.82 \times 10^9 \qquad (67)$$

and

$$A_3 = T\,A_3' = 1.38 \times 10^9,$$

where T = transmission through the LiH.

At the beginning of this section, it was said that the number of photons of some energy has no meaning, but for convenience we consider all the photons in the energy interval ("bin") $k \pm 1/2$ Mev to be of energy k. For instance, for type-1 film and the bin at 160 Mev, the "number of photons" is

$$N = \frac{\left(k\,\frac{d\sigma}{dk}\right)_{160} \times A}{160} = \frac{0.275 \times 23.53 \times 10^9}{160} = 0.404 \times 10^8. \qquad (68)$$

The $\left(k\,\frac{d\sigma}{dk}\right)_{160} = 0.275$ is the ordinate of curve III in Fig. 21 at 160 Mev.

VIII. CROSS-SECTION FORMULA

The differential cross section for some photon energy k and c.m. pion angle θ^* is related to the number of events seen in some solid-angle bin $\Delta\Omega^*$ and energy bin Δk as follows:

$$\Delta\Omega^* \, \Delta k \, \frac{d^2\sigma}{dk d\Omega^*} \times \left(\frac{\text{targets}}{\text{cm}^2}\right) \times (\text{photons of energy k}) \times (\text{chamber efficiency}) \tag{69}$$

$$= \sum_{\text{regions}=1}^{5} \frac{\text{events seen in region r in } \Delta k \Delta\Omega^*}{\text{scanning efficiency in region r}} .$$

The chamber efficiency is the fraction of events of some k and θ which are visible to the scanner. This is discussed in Sec. V. Notice that allowance is made for uneven scanning efficiencies by summing over various regions in the chamber.

An essential complication must be considered. The latitude allowed in operating conditions of the bubble chamber was approximately 1%. If the temperature dropped more than this limit, pions did not leave satisfactorily dense tracks, and if the temperature rose above this limit, the background obscured a large portion of the chamber. Therefore each picture was classified according to the appearance of the background in the beam region. These classification were:

Type 0. Chamber insensitive (cold).

Type 1. Obscuring background within two diverging planes 0.93 cm apart at center of chamber.

Type 2. Same as Type 1 except with a 1.98-cm separation.

Type 3. Same as Type 1 except with a 3.40-cm separation.

The angular separation of the planes was 8 deg and the dimensions are given in Fig. 9.

The inner-plane dimension was chosen so that 155-Mev events could be used. The outer-plane dimension was chosen where there was no noticeable drop in the distribution of muon ends and origins. The middle plane was placed arbitrarily.

The film was graded on the appearance of the electron background only. To avoid bias, we scanned at the rate of 2 or 3 pictures per second. The π-μ decays were not distinguishable at that speed and presumably did not affect our judgment of the film.

The relation relating the cross section to the number of events seen must be generalized to a sum over various film types i(i = 1, 2, 3). The geometrical chamber efficiency $\mathrm{Eff}(k, \theta)$ is different for each type of film so $\mathrm{Eff}(k, \theta) \rightarrow \mathrm{Eff}_i(k, \theta)$. Likewise the "number" of photons of energy k must be broken into the "number" which went through the chamber for pictures of type i.

$$\frac{d\sigma}{dk d\Omega^*} = \frac{\sum_{r=1}^{5} \frac{\text{events seen in region r in } \Delta\Omega\Delta k}{\text{scanning efficiency in region r}}}{\left(\frac{\text{targets}}{\text{cm}^2}\right) \times \sum_{i=1}^{3} (\text{photons})_i \times (\text{geometrical efficiency})_i \, \Delta\Omega^* \Delta k} \tag{70}$$

The number of targets/cm^2 is calculated in Sec. VI. The "number" of photons at each energy k is given in Sec. VII. The scanning efficiencies are listed in Sec. III.

IX. RESULTS

A. Gross Number of Events

A total of 529 rolls of film, of 400 pictures each, were taken. Of these, 138 were deemed unsatisfactory because of incorrect operating conditions of the chamber, unsatisfactory film developing, or of a failure in the illuminating system. The data of ten rolls were lost during an IBM 709 computer failure and it was felt that it wasn't worth running certain programs again to incorporate this data with the remainder. This left 381 rolls from which to calculate the cross section.

Nearly 5000 π-μ decays were seen by the scanners. About 600 of these were dropped because they didn't originate or end within the geometrical limits set up for the analysis. Thus we had 4400 events with which to work, but only 3400 of these were actually used, as will be seen.

B. Procedure for Calculating the Cross Section

The cross section was calculated by sorting out each event according to its c.m. angle, θ^*, and the lab energy, k, of the photon which produced it. We chose 20 angle bins at $\cos\theta^* = 0.95, 0.85, \cdots -0.85, -0.95$, and 32 energy bins at $k = 154, 155, \cdots 185$ Mev. The number actually added to the sum in a certain energy-angle bin was the inverse of the scanning efficiency for that particular event. Because the scanning efficiencies were around 99%, the number added was generally close to 1.01.

Thus we calculated the cross section according to Eq. (70), with the contents of each bin corresponding to the numerator of Eq. (70). After dividing the contents of each bin by the appropriate denominator according to Eq. (70), we had the differential cross section in cm^2/Mev-sr for pion photoproduction at a c.m. angle θ^* by photons of lab energy k.

C. Results

Table VII is a tabulation of the matrix element squared, $|M^2|$, in (μb/Mev-sr) where

$$\frac{d^2\sigma}{d\Omega^* dk} = \frac{p^*}{k^*} |M^2| \qquad (71)$$

p^* = c. m. pion momentum

k^* = c. m. photon momentum

A blank in the table represents bins in which there were no events. Table VIII is a list of the number of events in each bin.

There is a definite systematic error in Table VII, because for energies greater than 159 Mev, the measured cross section rises for forward angles and falls for backward angles. For energies below 159 Mev, the values fall for both forward and backward directions. However, for each energy, there is a set of angles for which the measured cross section is fairly constant. We are assuming that the true cross section should be isotropic at these energies and are confident that there isn't any phenomenon that would cause the angular distribution to rise or fall at forward and backward angles, yet be flat in the middle.

It is assumed that the error is caused by inaccurate geometrical efficiencies, which seems reasonable because it is difficult to estimate just exactly where in the background an event is visible and where it isn't. However, most of the data appear to be unaffected, and it is just for those types of events where the geometrical efficiency is substantially reduced because of the beam background that we must be selective. Just what portion of our data we consider valid is best seen by looking at Table VII.

The underlined numbers are those cross sections that we consider unaffected by inaccuracies in the geometrical efficiencies. For energies from 161 to 185 Mev, the regions of accuracy were chosen by looking at the geometrical efficiencies for each photon

Table VII. Measured values of the matrix element squared. Only the underlined values are valid. The pion c.m. angle is θ^*

	Laboratory photon energy (Mev)					
Cos θ^*	154	155	156	157	158	159
-0.95						
-0.85						
-0.75						
-0.65						8.72±4.36
-0.55			10.90±10.88		4.18±2.95	7.02±2.86
-0.45		15.07±14.97		5.00±3.53	(6.59±2.94)	(8.34±2.50)
-0.35				(4.81±2.77)	17.63±3.93	12.87±2.80
-0.25		5.68±5.67	(0)	10.22±3.40	13.51±3.18	15.82±2.99
-0.15		(3.06±3.04)	(7.03±3.51)	(11.53±3.33)	15.30±3.12	13.40±2.63
-0.05		(11.41±5.70)	(10.43±3.68)	17.61±3.75	10.91±2.57	10.56±2.25
0.05		13.61±5.12	18.02±4.64	12.64±3.16	10.40±2.39	5.54±1.48
0.15		14.55±5.49	14.02±3.74	15.24±3.24	15.95±3.01	12.34±2.37
0.25	(10.02±7.03)	9.82±3.90	10.65±3.21	14.53±3.25	11.06±2.21	14.08±2.76
0.35	16.50±8.25	14.60±5.16	19.20±4.10	17.61±3.45	12.27±2.79	12.09±2.52
0.45	6.04±4.26	10.87±4.11	17.61±4.14	9.06±2.61	13.95±2.73	12.49±3.03
0.55	31.62±12.82	9.49±3.58	13.43±3.47	13.83±3.17	18.31±3.40	8.47±2.55
0.65	(4.04±4.04)	11.80±4.82	13.62±4.11	15.23±3.81	5.56±1.85	14.50±3.87
0.75	(3.30±3.25)	10.51±4.30	14.57±4.04	14.04±3.62	17.50±4.12	4.05±2.02
0.85			1.06±1.06	(10.26±3.10)	(6.56±2.32)	11.20±3.73

Table VII. (continued)

Cos θ^*	Laboratory photon energy (Mev)					
	160	161	162	163	164	165
-0.95			0		13.93±8.04	3.00±3.00
-0.85		4.20±4.19	7.61±3.80	8.99±3.66	15.09±3.77	11.89±2.97
-0.75	11.81±5.26	10.35±4.21	15.62±3.90	14.74±3.29	12.93±2.64	13.77±2.60
-0.65	3.69±2.12	14.45±3.50	10.97±2.66	12.61±2.47	11.05±2.16	9.86±1.93
-0.55	4.34±1.77	14.01±2.80	10.42±2.13	12.22±2.16	14.54±2.27	14.02±2.11
-0.45	(5.32±1.68)	10.73±2.19	8.11±1.77	9.00±1.67	10.81±1.80	14.13±2.42
-0.35	19.20±3.07	11.02±2.10	10.20±1.75	15.78±2.35	13.42±2.53	17.11±3.35
-0.25	13.46±2.50	12.10±2.01	14.81±2.31	17.29±2.80	13.96±3.12	26.47±6.62
-0.15	12.92±2.12	15.98±2.46	22.51±3.22	20.97±3.77	42.60±8.35	31.24±18.03
-0.05	7.91±1.73	14.52±2.57	21.77±3.79	28.80±6.00	23.93±10.70	171.95±171.88
+0.05	19.76±2.94	18.39±3.25	17.01±3.80	58.93±17.01		
0.15	17.47±3.04	19.10±3.98	23.61±6.56	164.04±66.96		
0.25	18.59±3.65	23.34±5.10	29.83±9.94	172.33±121.83		
0.35	18.72±3.90	13.92±4.40	34.60±13.07			
0.45	22.78±5.10	29.50±9.83				
0.55	17.27±4.61	13.63±6.81				
0.65	22.86±6.89	57.82±28.90	25.60±25.59			
0.75	19.04±5.73	37.27±21.51				
0.85	9.88±5.70	428.42±302.82				

Table VII (continued)

Cos θ^*	Laboratory photon energy (Mev)					
	166	167	168	169	170	171
-0.95	11.52±4.68	16.66±5.25	13.22±3.81	7.81±2.59	16.10±3.43	12.63±2.75
-0.85	10.01±2.58	16.93±2.99	15.96±2.66	18.15±2.77	15.51±2.45	12.56±2.15
-0.75	16.80±2.66	17.58±2.56	15.34±2.37	14.08±2.05	11.88±2.04	13.10±2.35
-0.65	14.33±2.07	13.13±2.05	15.53±2.34	18.01±2.92	16.95±3.15	18.88±4.22
-0.55	12.99±2.16	18.31±2.97	19.25±3.57	30.25±6.31	25.75±9.73	131.72±76.03
-0.45	20.44±3.45	21.35±4.36	31.14±8.32	58.27±41.19		
-0.35	24.12±5.53	46.36±17.67				
-0.25	43.10±16.29					

There were no events in the remaining bins for these energies

Table VII (continued)

Cos θ^*	Laboratory photon energy (Mev)					
	172	173	174	175	176	177
-0.95	13.14±2.62	15.85±2.71	10.36±2.11	14.48±2.48	10.01±2.00	11.21±2.12
-0.85	11.54±1.90	16.20±2.44	17.33±2.61	10.66±2.27	17.16±3.36	19.67±4.29
-0.75	15.13±2.97	21.81±4.12	27.86±5.68	33.17±10.49	111.28±49.75	11222.57±6476.76
-0.65	24.02±6.42	62.98±23.79	329.39±190.16			
	There were no events in the remaining bins for these energies.					
	178	179	180	181	182	183
-0.95	11.95±2.18	6.57±1.64	10.59±2.12	14.22±2.73	7.17±2.16	10.53±3.33
-0.85	25.75±6.24	30.37±9.60	46.80±15.60	195.83±69.22	1304.60±1304.47	
	There were no events in the remaining bins for these energies.					
	184	185				
-0.95	21.70±6.01	11.60±6.70				
	There were no events in the remaining bins for these energies.					

Table VIII. Number of events in each energy-angle bin. Underlined numbers are the bins for which the differential cross sections are considered valid

	Photon Energy (Mev)																															
Cos θ^*	154	155	156	157	158	159	160	161	162	163	164	165	166	167	168	169	170	171	172	173	174	175	176	177	178	179	180	181	182	183	184	185
-0.95											3	1	6	10	12	9	22	21	25	34	24	34	25	28	30	16	25	27	11	10	13	3
-0.85								1	4	6	16	16	15	32	36	43	40	34	37	44	44	22	26	21	17	10	9	8	1	1		
-0.75							5	6	16	20	24	28	40	47	42	47	34	31	26	28	24	10	5	3								
-0.65						4	3	17	17	26	26	26	48	41	44	38	29	20	14	7	3	1										
-0.55			1		2	6	6	25	24	32	41	44	36	38	29	23	7	3													
-0.45		1		2	5	11	10	24	21	29	36	34	35	24	14	2			1													
-0.35				3	20	21	39	28	34	45	28	26	19	7		2																
-0.25		1		9	18	28	29	36	41	38	20	16	7																			
-0.15		1	4	12	24	26	37	42	49	31	26	3																				
-0.05		4	8	22	18	22	21	32	33	23	5	1																				
0.05		7	15	16	19	14	45	32	20	12	4	1																				
0.15		7	14	22	28	27	33	23	13	6																						
0.25	2	6	11	20	25	26	26	21	9	2																						
0.35	4	8	22	26	34	23	23	10	7																							
0.45	2	7	18	12	26	17	20	9																								
0.55	6	7	15	19	29	11	14	4																								
0.65	1	6	11	16	9	14	11	4	1																							
0.75	1	6	13	15	18	4	11	3																								
0.85	2	2	1	11	8	9	3	2																								
0.95	1			2	2	2																										

energy and accepting only that range of c. m. angle bins in which efficiencies were greater than one-half the maximum value. This can introduce no systematic error, because we consider only the relative angular distribution predicted by the geometrical efficiency, where the actual cross section is assumed to be isotropic.

For energies from 154 to 160 Mev, the procedure for selecting the range of c. m. angles not affected by error as the geometrical efficiency falls off is perhaps subject to a small systematic error of a percent or two favoring high cross sections. The limits were chosen wherever the actual distribution or the distribution predicted by geometrical efficiency fell off by a factor of two from the maximum. In Table VII, the numbers in parentheses represent the bins excluded by setting the limit at half maximum of the real distribution for energies from 154 to 160 Mev. It is felt that, as a whole, these numbers are significantly too low and would cause a systematic error if used to represent the cross section. Therefore only those cross sections underlined in Table VII are considered valid.

Figures 23, 24, and 25 show the c. m. angular distributions for k = 156, 160, and 164 Mev. As would be expected at these energies, the distributions appear isotropic. In view of this isotropy, we can improve the statistics by averaging the cross section over c. m. angles.

Because the probability of producing a photopion has a Poisson distribution, we cannot average the entries in Table VII over angle but must separately average over angles the numerator and denominator of Eq. (70). That is, we now are considering only 32 energy bins regardless of the c. m. angle of the events. Equation (70) becomes

$$\frac{d^2\sigma}{dk\,d\Omega^*} = \frac{\sum_{r=1}^{5} \dfrac{\text{events of energy k in region r in range of acceptable angles}}{\text{scan efficiency in region r}}}{(\text{targets/cm}^2) \sum_{i=1}^{3} (\text{photons})_i \cdot \Delta k \cdot \int \text{geometrical eff. } d\Omega^*} , \tag{72}$$

where i is the type 1, 2, or 3 film, and r is the 1, 2, 3, 4, or 5, scanning region. The bin width is 1 Mev.

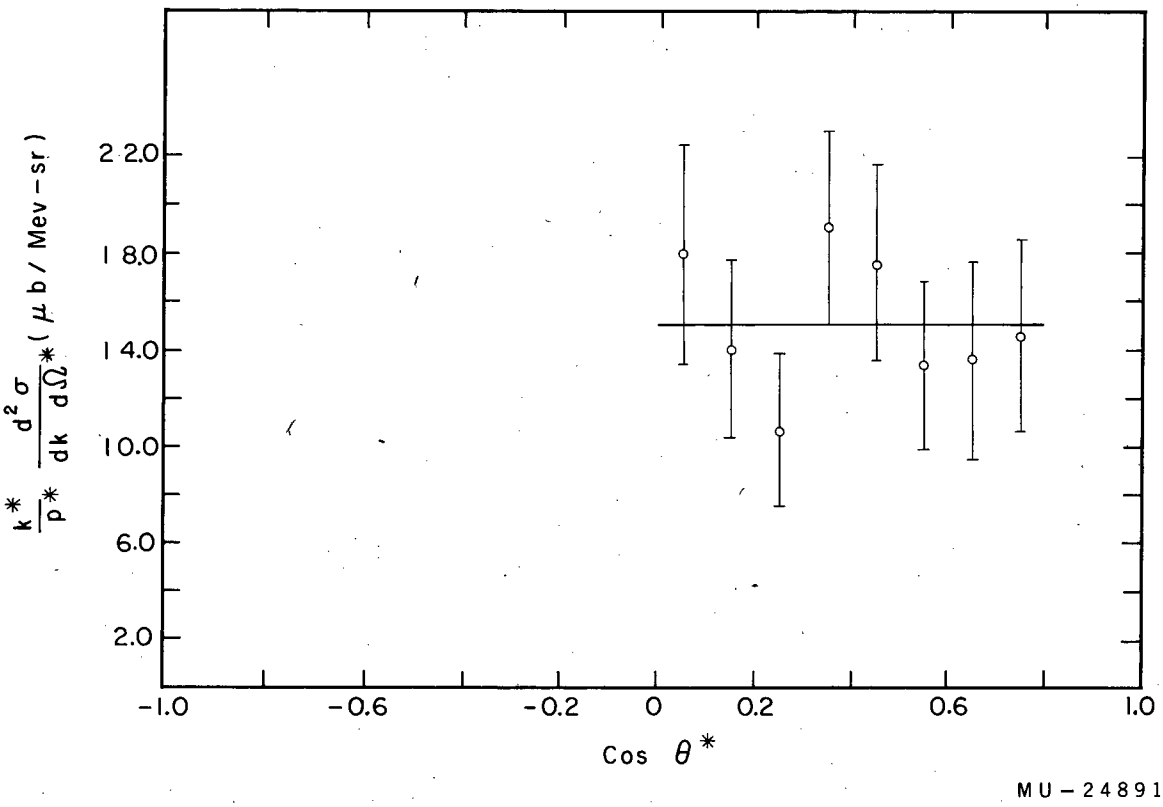

Fig. 23. Angular distribution of the matrix element squared for photopions produced by 156-Mev photons. Errors are counting errors only. The solid line is the average of the data.

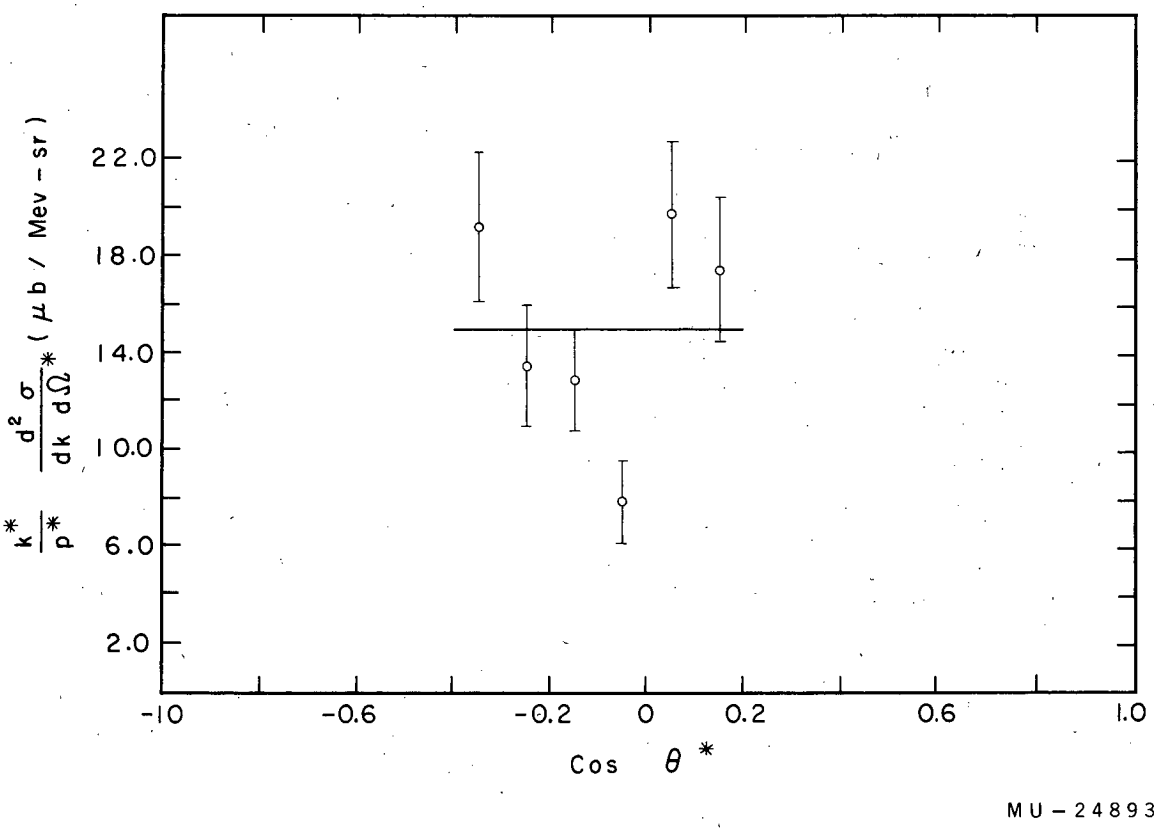

Fig. 24. Angular distribution for the matrix element squared for photopions produced by 160-Mev photons. Errors are counting errors only. The solid line is the average of the data.

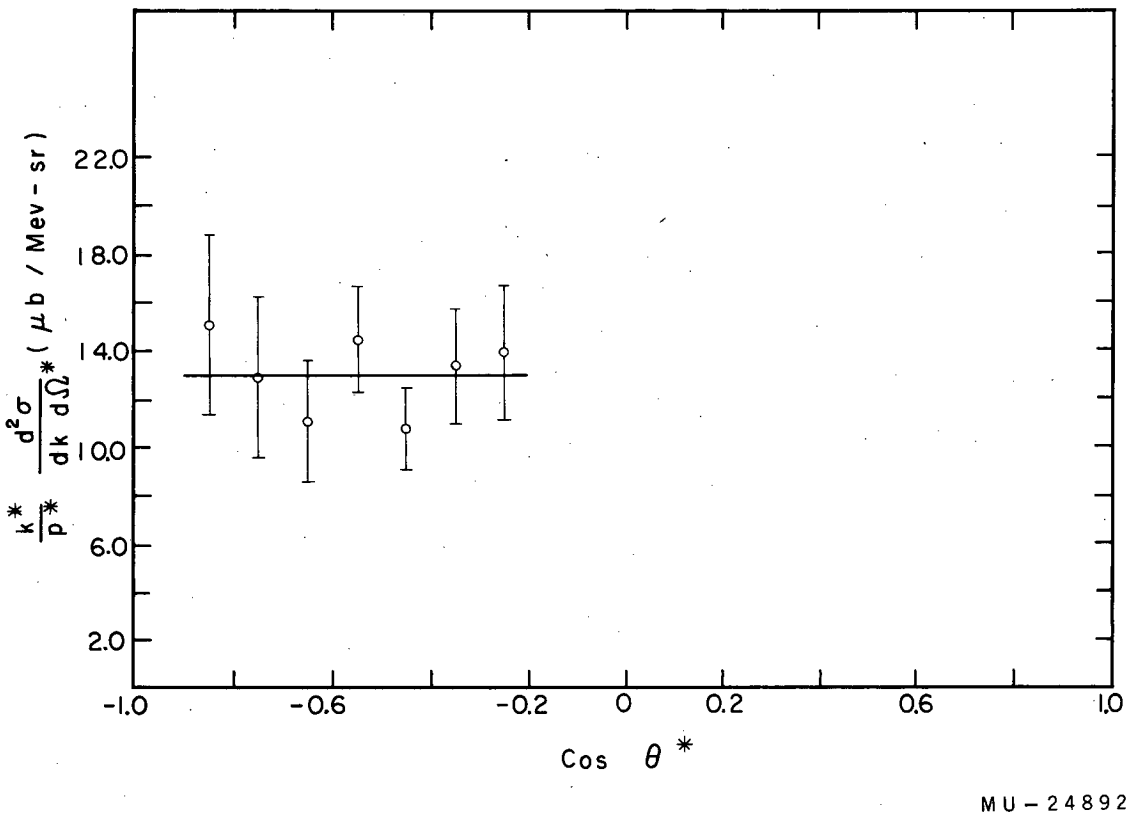

Fig. 25. Angular distribution for the matrix element squared for photopions produced by 164-Mev photons. Errors are counting errors only. The solid line is the average of the data.

Figure 26 shows the average matrix element squared versus lab photon energy. As before, the ordinates are the actual cross sections multiplied by the kinematic factor k^*/p^*. The errors are counting errors only. The solid line in Fig. 26 is the theoretical cross section calculated by Ball with the scaling factor $\Lambda = 0$. The two dashed lines represent the cross section with $\Lambda = \pm 1.8$ e. Previous experimental points are included as noted on the figure. Table IX gives the data plotted in Fig. 26; the column labeled "Weight" is the denominator of Eq. (72) multiplied by p^*/k^*.

D. Normalization Error

The errors quoted in Table VII and Figs. 23 through 26 are counting errors. The relative counting error on the cross section for each energy-angle bin is $1/\sqrt{N}$, the inverse square root of the number of events in the bin. In addition, there is an error inherent in the normalization of the beam.

In Sec. VII four parameters were used to normalize the beam, namely:

Peak energy = 189.1 ± 3.7 Mev
LiH transmission = 0.5116 ± 0.0005
LiH in-out ratio = 0.484 ± 0.007
Cornell chamber response =
$(3.830 \pm 0.118) \times 10^{18}$ Mev/coul.

The errors on these parameters constitute a relative error of 4.1% on all cross sections in addition to the counting errors. This normalization error was not included with the data, because it is correlated since it affects the data as a whole. That is, if there is an error in the normalization, all the data should be increased or decreased without any relative change.

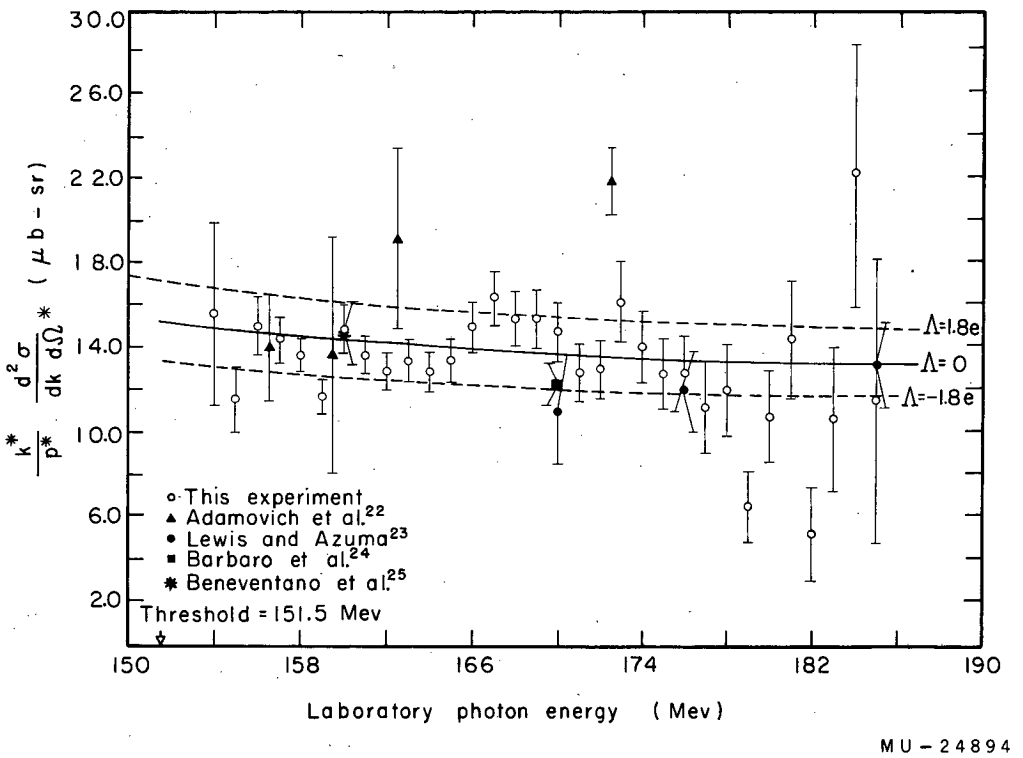

Fig. 26. Matrix element squared, averaged over c.m. angles, versus photon energy. Errors are counting errors only and all data are subject to correlated normalization error of 4.1%

Table IX. Matrix element squared, averaged over c. m. angles

Laboratory photon energy (Mev)	Weight (Mev-sr/cm^2)	Matrix element squared (cm^2/Mev-sr)
154	0.7656	15.74±4.34
155	4.624	11.70±1.59
156	7.865	15.15±1.39
157	11.62	14.48±1.11
158	19.47	13.80±0.84
159	18.24	11.80±0.80
160	13.61	15.00±1.05
161	17.02	13.88±0.90
162	15.52	13.02±0.92
163	14.07	13.51±0.98
164	14.72	12.98±0.94
165	12.87	13.53±1.02
166	11.50	15.14±1.15
167	9.61	16.46±1.31
168	8.63	15.54±1.34
169	8.83	15.53±1.33
170	8.38	14.93±1.33
171	6.637	12.96±1.40
172	6.709	13.13±1.40
173	4.787	16.31±1.85
174	4.793	14.20±1.72
175	4.351	12.88±1.72
176	3.942	12.94±1.81
177	2.464	11.34±2.15
178	2.470	12.15±2.22
179	2.394	6.69±1.67
180	2.303	10.86±2.17
181	1.855	14.57±2.80
182	1.496	7.35±2.22
183	0.925	10.81±3.42
184	0.582	22.35±6.20
185	0.259	11.60±6.70

E. Value of the Parameter Λ

We fit the theory to the data by adjusting the value of the parameter Λ. This parameter is discussed in Sec. I and is the multiplicative constant of the matrix element for pion photoproduction from a pion into a final state of angular momentum 1.

The fitting procedure must be compatible with the statistical distribution of the data. First we condense Eq. (72) into the form

$$\frac{k^*}{p^*}\,\frac{d\sigma}{dk^* d\Omega^*} = |M_k|^2 = \frac{N_k}{W_k}\ ;\ k = 154 \cdots 185. \qquad (73)$$

The numerator N_k is the sum of all events of energy k (actually the sum of the inverses of the scanning efficiency for each event), and the denominator W_k is the appropriate weighting factor. The product $|M_k|^2 W_k$ is Poisson-distributed; so the probability for measuring some particular $|M_k|^2$ is

$$P(N_k, |M_k|^2) = \frac{(|M_k|^2 W_k)^{N_k}}{N_k!}\, e^{-|M_k|^2 W_k}. \qquad (74)$$

From Sec. I, we know that

$$|M_k|^2 = \left(1 + \frac{0.074\Lambda}{e}\right)|M_k'|^2, \qquad (75)$$

where the matrix element $|M_k'|^2$ for the photopion production from nucleons alone is given by Ball. Using the $|M_k'|^2$ and knowing the probability $P(M_k, |M_k|^2)$, we can calculate the most probable Λ from

$$1.0 + \frac{0.074\Lambda}{e} = \frac{\sum_{k=1}^{32} N_k}{\sum_{k=1}^{32} W_k |M_k'|^2} = \frac{3351}{3452} = 0.9707, \qquad (76)$$

which gives $\Lambda = -0.397$. The sum over k = 1, 2 $\cdots$ 32 is the sum over the 32 energy bins.

The true error on $0.074\Lambda/e$ is the relative normalization error 0.041 of paragraph D of this section. Thus the error on Λ is due to the normalization error only, and we have

$$\Lambda = (-0.397 \pm 0.552)e.$$

The effect of the counting statistics on the error of Λ is negligible, since 3351 events were used.

Further measurement of π^+ cross sections cannot improve the error on Λ until more accurate calibration of photon beams is effected. Ball notes that this method also subjects Λ to the error on the pion-nucleon coupling constant $f^2 = 0.08$ which he used in calculating the theoretical cross section displayed in Fig. 26. He further states that the (π^-/π^+) ratio is not beset by these normalization difficulties but that the experimental uncertainty in the -/+ ratio is considerable.

F. Conclusions

The results of this section are briefly summarized here. Figures 23, 24, and 25 show that the measured angular distributions are consistent with isotropy, which is in agreement with the prediction that near threshold the process is primarily electric-dipole into a final s-wave state.

Table IX shows the squares of the matrix elements averaged over the c.m. angle of the pion. These data, which are plotted in Fig. 26 show that the variation with photon energy and the magnitudes of the matrix element squared are in good agreement with the theoretical calculations of Ball.[3] In addition, there is good agreement with the previous experimental data, except for the 172.5-Mev point of Adamovich et al.[22]

Finally, the value obtained for the parameter Λ shows that the effect of the $\pi + \gamma \rightarrow N + \bar{N}$ channel on the reaction studied here is small.

ACKNOWLEDGMENTS

The experimental run was conducted in the summer of 1959. During the run and the succeeding two years, many people contributed to this paper and I wish to express my gratitude here.

First, I thank Dr. Robert Kenney for suggesting the experiment and for giving me confidence at various stages of the data analysis. Many times in the past years, I have called upon Professor A. C. Helmholz for assistance and advice which I appreciated.

Drs. Duane Gates and William Swanson aided during the run and were helpful afterwards. The synchrotron crew, which has long since been disbanded, extended themselves so that we could run twenty-four hours a day rather than the usual sixteen. This allowed us to stabilize the operating conditions of the chamber.

The bubble chamber and film-analyzing equipment were loaned to us by Professor Luis Alvarez. Mr. Arthur Barnes designed and supervised the construction of a new measuring machine when our old one failed in the midst of the analysis.

The exacting scanning and measuring work was done by Messrs. Raymond Walker, Joseph Hirsch, Charles Welsh, Gerald Belanger, and Lee Fisher, and Misses Betty Blaine and Olga Fekula. Much of the data analysis was supervised by Lt. Remington Stone. I am grateful for the patience exhibited by the operators of the 709 computer at my initial attempt at a large-scale data-analysis problem.

Miss Miriam Machlis did all the typing and was helpful in setting up the paper in its final form.

Finally, I wish to thank my wife, Jeannie, and my parents, Mr. and Mrs. Leo McPherson for their support during my years as a graduate student.

This work was done under the auspices of the U. S. Atomic Energy Commission.

REFERENCES

1. G. F. Chew and F. E. Low, Phys. Rev. 101, 1579 (1956).
2. G. F. Chew, M. L. Goldberger, F. E. Low, and Y. Nambu, Phys. Rev. 106, 1345 (1957).
3. J. S. Ball, Phys. Rev. Letters 5, 73 (1960). A more detailed account is given in "The Application of the Mandelstam Representation to Photoproduction of Pions from Nucleons," UCRL-9172, April 11, 1960.
4. How-sen Wong, Phys. Rev. Letters 5, 70 (1960). A more detailed account is given in "Low-energy Photopion Production from Pions and Neutral Pion Decay," UCRL-9251, June 2, 1960.
5. W. R. Frazer and J. R. Fulco, Phys. Rev. 117, 1609 (1960).
6. W. R. Frazer and J. R. Fulco, Phys. Rev. 117, 1603 (1960).
7. D. C. Gates, R. W. Kenney, D. A. McPherson, and W. P. Swanson, Rev. Sci. Instr. 31, 565 (1960).
8. D. H. Miller and D. A. Hill, Lawrence Radiation Laboratory, private communication through R. W. Kenney, Lawrence Radiation Laboratory.
9. D. C. Gates, "Electron Triplet Production by High-Energy Photons in Hydrogen," UCRL-9390, Sept. 1, 1960, (submitted to Phys. Rev.).
10. D. R. Corson, J. W. DeWire, B. D. McDaniel, and R. R. Wilson, "The Cornell 300-Mev Synchrotron," Office of Naval Research Report NP4972, July 1953.
11. D. Parmentier, Jr., and A. J. Schwemin, Rev. Sci. Instr. 26, 954 (1955).
12. L. Reed and R. Tripp, "Density of Hydrogen at Operation Conditions of 15-inch Bubble Chamber," LRL Engineering Note 4320-01M2, Oct. 1958.
13. W. Whaling, Encyclopedia of Physics, Vol. 34 (Springer Verlag, Berlin, 1958), p. 208.
14. W. A. Aron, "The Passage of Charged Particles through Matter" (Thesis) UCRL-1325, May 1951.

15. W. Whaling, California Institute of Technology, Pasadena, private communication.
16. R. D. Evans, The Atomic Nucleus (McGraw-Hill Book Co., New York, N. Y. 1955), Chap. 22, p. 660.
17. F. J. Loeffler, T. R. Palfrey, and G. W. Tautfest, Nucl. Instr. and Methods 5, 50 (1959).
18. H. Olsen and L. C. Maximon, Phys. Rev. 114, 887 (1959).
19. H. W. Koch and J. W. Motz, Revs. Modern Phys. 31, 929 (1959). (This is a complete review of bremsstrahlung cross sections.)
20. E. Hisdal, Phys. Rev. 105, 1821 (1957).
21. R. Wilson, Proc. Phys. Soc. (London) A66, 638 (1953).
22. M. I. Adamovich, E. G. Gorzhevskaya, V. G. Larionova, V. M. Popova, S. P. Kharlamov, and F. R. Yagudina, J. Exptl. Theoret. Phys. (S. S. S. R.) 38, (1960) [Translation: Soviet Phys. JETP 11, 779 (1960)].
23. G. M. Lewis and R. E. Azuma, Proc. Phys. Soc. (London) A73, 873 (1959).
24. A. Barbaro, E. L. Goldwasser, and D. Carlson-Lee, Bull. Am. Phys. Soc., Ser. II, 4, 273 (1959).
25. M. Benevantano, G. Bernardini, D. Carlson-Lee, G. Stoppini, and L. Tau, Nuovo cimento 4, 323 (1956).